CAIQUE DIAS LUKO

Topographically-generated submesoscale shear instabilities associated with Brazil Current meanders

São Paulo

2022

CAIQUE DIAS LUKO

Topographically-generated submesoscale shear instabilities associated with Brazil Current meanders

A thesis submitted to the Instituto Oceanográfico of the Universidade de São Paulo in partial fulfilment for the degree of Master of Science in Oceanography, with emphasis in Physical Oceanography.

Advisor: Prof. Dr. Ilson Carlos Almeida da Silveira

São Paulo

2022

Luko, Caique Dias. **Topographically-generated submesoscale shear instabilities associated with Brazil Current meanders**. A thesis submitted to the Instituto Oceanográfico of the Universidade de São Paulo in partial fulfilment for the degree of Master of Science in Oceanography, with emphasis in Physical Oceanography.

Approved on 04/29/2022

Corrected version

Judging Committee

Prof PhD _____ Institution _____

Grade _____ Signature _____

Prof PhD _____ Institution _____

Grade _____ Signature _____

Prof PhD _____ Institution _____

Grade _____ Signature _____

Acknowledgments

It is with great joy that I deliver this Master's thesis! It represents a lot of what I love about oceanography. It's funny how life has brought me here. An unlikely path that made me find a profession I'm passionate about. Many people were responsible for getting me into the University and helped me through my Master's.

First of all, I want to thank all my family for their support. In particular, I would like to thank my mother. She dreamed that I could study at USP, and she worked hard to give me this opportunity. If it was not for her, I would not have gotten here.

A special acknowledgment also goes to the Professors I had during my undergraduate and graduate years at IOUSP. Specifically, I thank my advisor Prof. Ilson Carlos Almeida da Silveira. Ilson, if it weren't for the time dedicated to discussing science, and if it weren't for the many opportunities you gave me, I'm sure I wouldn't be able to produce this work. Just like Prof. Ilson, I want to thank Prof. Amit Tandon. Both of you helped me grow academically and helped me find what I love to do. Finally, I also thank Cauê Lazaneo and Filipe Pereira who were practically my Professors while collaborating with me on my Bachelor's and Master's thesis. I learned a lot from you guys.

I would also like to send a special hug for the friends from the XIV-IOUSP cohort, LaDO, and the Upper Ocean Physics Laboratory: Felipe Vilela, Pedro Walfir, Gabriel Lucas, Henrique Rodrigues, Bruno Pegoraro, Natália Silva, Santiago Bravo, Cauê Lazaneo, Filipe Pereira, Adriano Giangiardi, João Pedro, Milton, Dante Napolitano, Iury Souza, Ágata Piffer, Igor Uchôa, Siddhant Kerhalkar and all the others with whom I lived. Thank you very much! These years became much more fun with you.

I cannot forget to acknowledge the support from IOUSP's employees. Special thanks to Eder, Ricardo, Silvana, Ana Paula, Daniel, Leticia, Marta and Wagner that made life way easier during the pandemic. Finally, I acknowledge the financial support from FAPESP (Proc. number: 2020/04124-0) and CNPQ (Proc. number: 130288/2020-9).

Thank you everyone! This work has the contribution of all of you!

"O tempo às vezes é alheio à nossa vontade
Mas só o que é bom dura tempo o bastante
Para se tornar inesquecível"

– Charlie Brown Jr.

Resumo

Luko, Caique Dias. **Instabilidades de cisalhamento em submesoescala associadas a interação de meandros da Corrente do Brasil com a topografia**. 2022. Dissertação de Mestrado - Instituto Oceanográfico, Universidade de São Paulo, São Paulo.

Ao largo da costa sudeste brasileira, um jato de primeiro modo baroclínico é observado acima do talude continental: a Corrente do Brasil (CB) que escoa para o sul e ocupa os primeiros 200-300 m de coluna d'água, e a Corrente de Contorno Intermediária (CCI) que escoa para o norte e se estende de ∼200-300 m a ∼1800 m. Entre 22° e 23°S, o jato CB-CCI desenvolve recorrentes meandros ciclônicos que crescem quase-estacionariamente via instabilidade baroclínica. Estes meandros aumentam a produtividade primária no oceano aberto e são importantes para a sociedade, já que se formam em uma região rica em petróleo e gás, onde já ocorreram acidentes de derramamento de óleo. Neste estudo, pretendemos explorar os processos responsáveis por desencadear a formação desses vórtices de mesoescala, adicionando a componente de submesoescala ao cenário hidrodinâmico. Para isso, uma simulação numérica de resolução de 2 km é realizada com o modelo CROCO. Os resultados indicam que anticiclones vindos de leste atingem o talude a montante de regiões de separação, e geram instabilidade barotrópica de submesoescala que desencadeia a formação dos meandros. Posteriormente, ciclones de submesoescala são gerados e contribuem, juntamente com a instabilidade baroclínica, para o crescimento dos meandros em uma cascata inversa da submesoescala para a mesoescala. Por fim, à medida que os ciclones de mesoescala crescem, eles interagem com o talude e geram vórtices anticiclônicos de submesoescala e filamentos que são inercial- e simetricamente instáveis.

Palavras-chave: Corrente do Brasil, Ciclone de Cabo de São Tomé, Ciclone de Cabo Frio, Instabilidade Barotrópica, Cascata Inversa, Vórtices Coerentes de Submesoescala.

Abstract

Luko, Caique Dias. **Topographically-generated submesoscale shear instabilities associated with Brazil Current meanders**. 2022. Master's Thesis - Oceanographic Institute, University of Sao Paulo, Sao Paulo.

Off southeastern Brazil, a unique first-mode-like baroclinic jet is observed above the continental slope: the southward flowing Brazil Current (BC) which occupies the upper 200-300 m, and the northward flowing Intermediate Western Boundary Current (IWBC) which spans from ∼200-300 m to ∼1800 m. Between 22° and 23°S, the BC-IWBC jet develops recurrent cyclonic meanders that grow quasi-stationarily via baroclinic instability. Such meanders enhance the open-ocean primary productivity and are of societal importance as they are located in a region rich in oil and gas where oil-spill accidents have already happened. Here, we aim to further explore the processes responsible for triggering the formation of these mesoscale eddies by adding the submesoscale component to the hydrodynamic scenario. To address this, a 2-km resolution numerical simulation is performed with CROCO. Our results indicate that incoming anticyclones reach the slope upstream of separation regions and generate submesoscale barotropic shear instability that trigger the meanders' formation. Subsequently, this process generates submesoscale cyclones that contribute, along with baroclinic instability, to the meanders' growth resulting in a submesoscale-mesoscale inverse cascade. Lastly, as the mesoscale cyclones grow, they interact with the slope generating anticyclonic submesoscale vortices and filaments that are inertially and symmetrically unstable.

Key-words: Brazil Current, Cape São Tomé Cyclone, Cape Frio Cyclone, Barotropic Instability, Inverse cascade, Submesoscale Coherent Vortices.

List of Figures

List of Tables

Acronyms

AAIW	Antarctic Intermediate Water
BC	Brazil Current
CF	Cape Frio
CROCO	Coastal Regional Oceanic COmmunity model
CST	Cape São Tomé
DWBC	Deep Western Boundary Current
G	Gravitational
I	Inertial
IWBC	Intermediate Western Boundary Current
JAMSTEC	Japan Agency for Marine-Earth Science and Technology
KPP	K-profile parameterisation
NBUC	North Brazil Undercurrent
OfES	OGCM for the Earth Simulator
OGCM	Ocean General Circulation Model
PDF	Probability Density Function
S	Symmetric
SACW	South Atlantic Central Water
SCVs	Submesoscale Coherent Vortices
St.	Stable
WOA18	World Ocean Atlas 2018

Symbols

Ro	Rossby number
Ri	Richardson number
ζ	Relative vorticity
f	Planetary vorticity
T	Temperature
h	CROCO Topography
q	Potential vorticity
ω_a	Absolute vorticity
b	Buoyancy
N^2	Stratification
x	Zonal distance
y	Meridional distance
z	Vertical distance
u	Zonal velocity
v	Meridional velocity
w	Vertical velocity
ϕ_{tw}	Thermal wind Thomas angle
ϕ_{tw_c}	Thermal wind critical Thomas angle
Ri_B	Bulk Richardson number
ζ_g	Geostrophic relative vorticity
Cu	Curvature number
r	Local radius of curvature
ϕ_{gw}	Gradient wind Thomas angle
ϕ_{gw_c}	Gradient wind critical Thomas angle
KE	Kinetic Energy
MKE	Mean Kinetic Energy
MPE	Mean Potential Energy
EKE	Eddy Kinetic Energy
EPE	Eddy Potential Energy

HSP	Horizontal Shear Production
BP	Buoyancy Production
BF	Buoyancy Flux
A	Normalization area
L	Diameter of normalization area
R	Radial position vector
ρ_0	Mean density
Π	Kinetic Energy Flux across scales
α	Strain
δ	Divergence
M^2	Buoyancy horizontal gradient

Contents

1 Introduction

This thesis investigates the development of topographically-generated submesoscale shear instabilities associated with Brazil Current (BC) meanders. In the following sections, we: i) give a brief overview on topographically-generated submesoscale motions; ii) review the literature about the BC and its meanders, and; iii) formulate the scientific questions and present the objectives to achieve our goals.

1.1 Topographically-generated submesoscale motions

Submesoscale currents are dynamically distinguished by their Rossby (Ro) and Richardson (Ri) numbers that reach $\mathcal{O}(1)$ values (Thomas et al., 2008; McWilliams, 2016; Gula et al., 2022). Such phenomena occur in the transition between the two-dimensional quasi-geostrophic mesoscale and the isotropic small scale, assuming horizontal scales of 100 m - 10 km and time scales of hours to weeks (Thomas et al., 2008; McWilliams, 2016). For a long time, the investigation of submesoscale motions encountered an operational barrier due to their length scales. However, increased spatial resolution in both observations and modeling has shown the abundance of submesoscale processes as well as their importance: i) to cascade energy from the mesoscale to energy dissipation scales (Müller et al., 2005); ii) to restratify the upper-ocean (Fox-Kemper et al., 2008); and iii) to the vertical exchange of tracers and, consequently, to structure marine ecosystems (Mahadevan, 2016; Lévy et al., 2018; Fadeev et al., 2021).

Submesoscale motions can arise through mixed layer baroclinic instabilities, mesoscale strain leading to frontogenesis, atmospheric destabilizing forcing, and flow interactions with topography (Gula et al., 2022). In particular, submesoscale motions generated by flow-topography interactions can play a key role in the generation of mesoscale meanders downstream of separation regions. Off the United States (US) East Coast, for instance, the Gulf Stream crosses the Charleston Bump and generates barotropic shear instability (Gula et al., 2016a). During this process, submesoscale cyclones are ejected offshore, and subsequently, mesoscale meanders

grow downstream (Figure 1.1). By contrast, off the US West Coast, the California Undercurrent generates inertial instability while crossing separation regions (Molemaker et al., 2015). Subsequently, submesoscale anticyclones are ejected offshore and contribute to the growth of mesoscale anticyclones in a submesoscale-to-mesoscale inverse cascade.

Submesoscale motions can trigger the formation of mesoscale meanders, but the opposite is also true. The interaction of mesoscale meanders with topography can ignite symmetric and inertial instabilities (Napolitano et al., 2021a), and generate Submesoscale Coherent Vortices (SCVs) (Lazaneo et al., 2022). Such processes can enhance the vertical exchange of tracers and lead to energy dissipation (Gula et al., 2016b; Lazaneo et al., 2022).

Off southeastern Brazil, BC cyclones are generated downstream of separation regions, and grow quasi-stationarily adjacent to the shelf-break (Silveira et al., 2008). Thus, submesoscale flow-topography processes might be important to both: i) the generation of the regional meanders, and; ii) the development of symmetric/inertial instabilities, and subsequent formation of SCVs.

1.2 The Brazil Current and its meanders

The Brazil Current is the western boundary current that closes the South Atlantic Subtropical Gyre (Stramma & England, 1999). The BC arises at the surface South Equatorial Current branch bifurcation at about 14°S as a mixed-layer southward jet that transports Tropical Water (Rodrigues et al., 2007; Soutelino et al., 2011; Luko et al., 2021). It increases its vertical extension and transport as it receives the inflow of South Atlantic Central Water (SACW) and Antarctic Intermediate Water (AAIW) coming from different impinging South Equatorial Current bands (Figure 1.2a, Soutelino et al., 2011; Luko et al., 2021). For instance, at about 23°S, the BC occupies the upper ∼350 m and transports 1-5 Sv, while south of 27°S it spans the upper ∼800 m and transports 10-20 Sv (Figure 1.2b, Rocha et al., 2014; Schmid & Majumder, 2018).

Off southeastern Brazil, we observe a unique first-mode like baroclinic jet above the continental slope: the BC occupies the upper 200-350 m, while the underlying northward-flowing Intermediate Western Boundary Current (IWBC) spans from ∼200-350 m to ∼1800 m (Figure 1.3, Silveira et al., 2004; Napolitano et al., 2019). With this configuration, the BC-IWBC jet dissipates energy due to intense vertical shear (Lazaneo et al., 2020), and develops recurrent

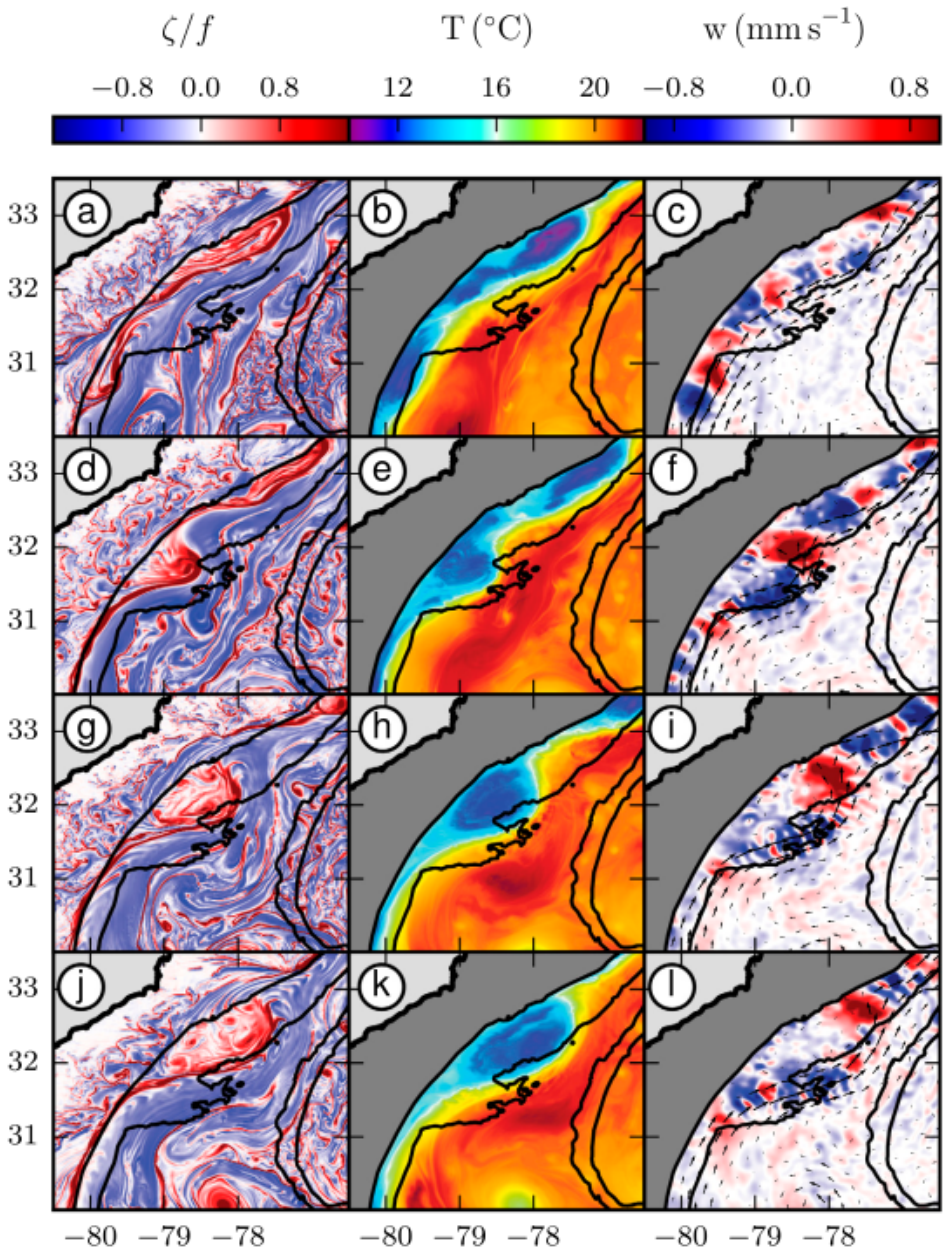

Figure 1.1: The formation of a large frontal Gulf Stream eddy in snapshots of (left) surface relative vorticity (ζ) normalized by f, (center) temperature at z = -200 m, and (right) vertical velocity at z = -200 m. The time interval between consecutive rows is 3.5 days. Topography is shown in black contours for the levels -200, -600, -1000, and -2000 m. Extracted from Gula et al. (2016a).

mesoscale meanders through baroclinic instability (Silveira et al., 2008; Rocha et al., 2014). These meanders are known to play a key role in coastal upwelling (Calado et al., 2010; Palóczy

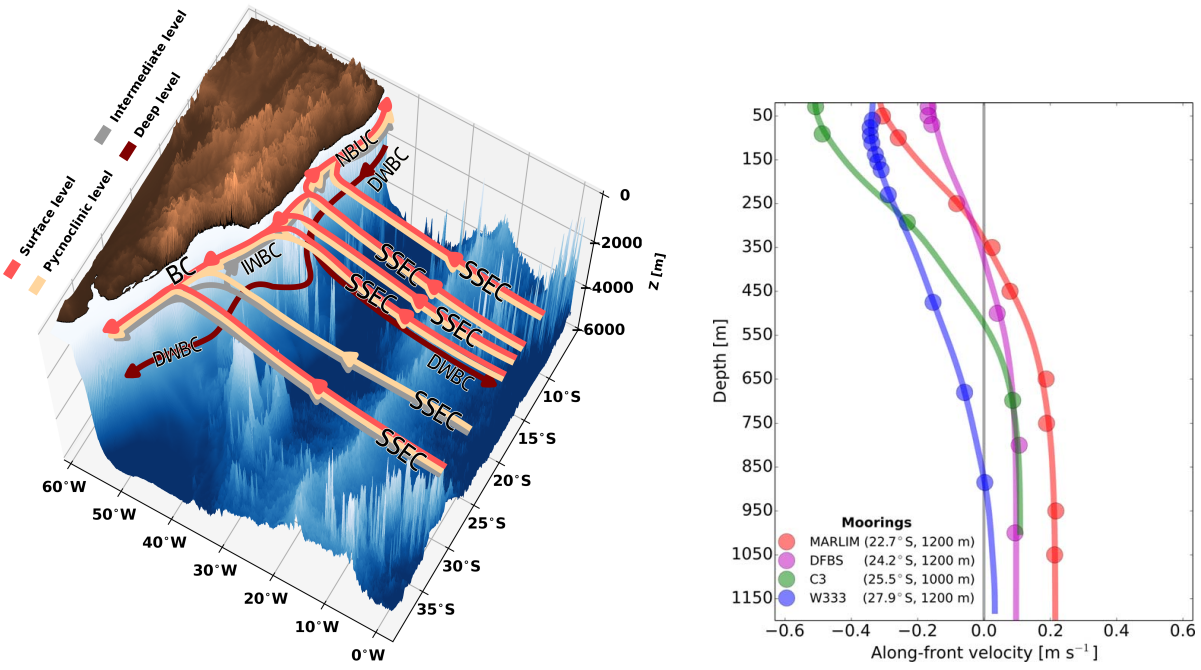

(a) Luko et al. (2021) **(b)** Rocha et al. (2014)

Figure 1.2: a) South Equatorial Current pathway throughout the South Atlantic. Extracted from Luko et al. (2021). b) Time mean along-front velocity ($m\,s^{-1}$) for the moorings: MARLIM (22.7°S, red); DFBS (24.15°S, magenta); C3 (25.5°S, green), and W333 (27.9°, blue). Extracted from Rocha et al. (2014). NBUC: North Brazil Undercurrent; IWBC: Intermediate Western Boundary Current; DWBC: Deep Western Boundary Current.

et al., 2014), in transporting shelf waters to the open ocean (Mill et al., 2015), and in modulating the regional biogeochemical dynamics (Figure 1.4, Pereira et al., 2019).

The BC is prone to baroclinic instability from 20°S to 36°S (Magalhães et al., 2017). However, stronger mesoscale activity is observed off southeastern Brazil as the BC crosses two separation regions: i) Cape São Tomé (CST, ∼22°S) and, ii) Cape Frio (CF, ∼23°S). As the BC crosses these capes, barotropic instabilities happen upstream, while baroclinic instabilities happen downstream (Magalhães et al., 2017).

As seen in the last section, topographically-generated submesoscale shear instabilities can contribute to the formation and to the growth of mesoscale meanders. To our knowledge, there are no studies that investigate the role of submesoscale motions on the BC meanders dynamics. Consequently, there is also no information on how the submesoscale relates to the barotropic

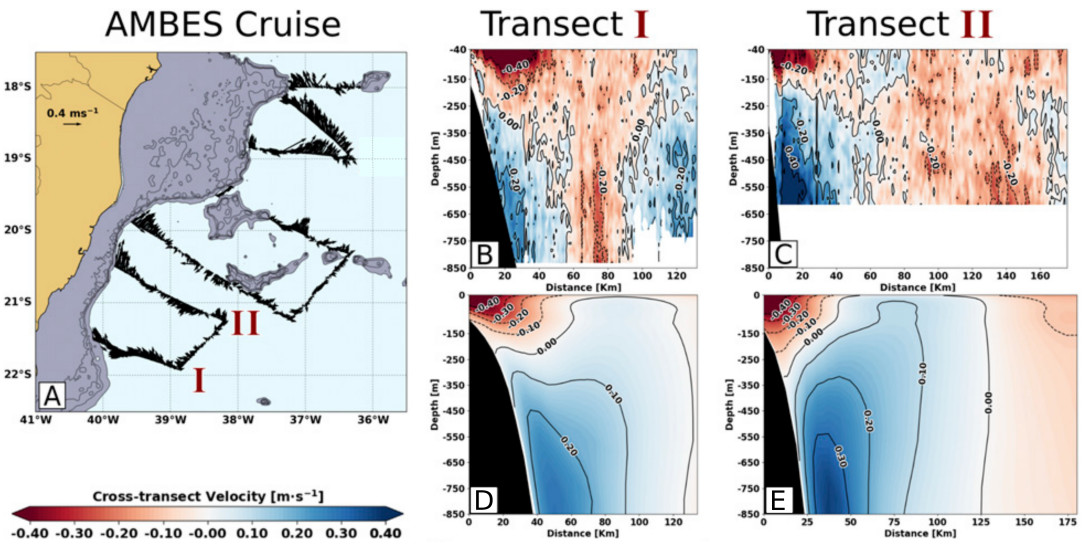

Figure 1.3: BC and IWBC vertical structure observed off southeastern Brazil (adapted from Napolitano et al. (2019)). (a) Horizontal circulation pattern at 600 m from shipboard ADCP data obtained during the AMBES cruise (5–18 Oct 2012; black arrows). (b)–(c) Shipboard ADCP vertical sections from transects I and II of the AMBES campaign. (d)–(e) ROMS 2-month averages (September–October) for the 7 years of simulation at transects I and II. Solid (dashed) black contours represent equatorward (poleward) velocities.

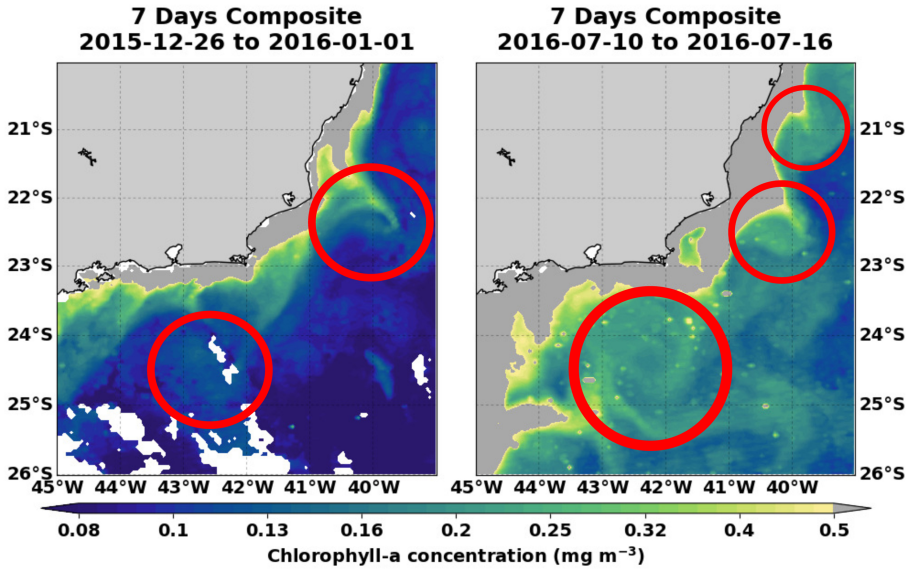

Figure 1.4: Chlorophyll-a concentration maps extracted from Pereira et al. (2019). Red circles mark the BC cyclonic eddies.

and baroclinic instabilities observed in mesoscale studies.

1.3 Scientific questions and objectives

Based on the literature review, we formulate the following scientific questions:

- Do submesoscale shear instabilities generated by flow-topography interactions play a role in the formation of BC meanders between 22°S and 23°S?
- Do submesoscale features generated by shear instabilities contribute to the growth of the BC meanders in a submesoscale-to-mesoscale inverse cacade (e.g., Molemaker et al., 2015)?
- Does the interaction of the BC cyclones with topography generate submesoscale instabilities and submesoscale vortices?

In summary, the main objective of this thesis is to investigate if there is any occurrence of topographically-generated submesoscale shear instabilities associated with BC meanders. To achieve that, we analyze the outputs of a submesoscale-permitting CROCO simulation. To answer to each of the scientific questions, we also formulate the following specific objectives:

- To analyze the temporal evolution of the Rossby number, potential vorticity, and energy conversion terms to find regions where submesoscale barotropic instabilities might occur;
- To perform a Kinetic Energy flux analysis to determine if a submesoscale-to-mesoscale inverse cascade contribute to the growth of the BC meanders, and;
- To verify if flow-topography interactions generate inertial/symmetric instabilities and submesoscale vortices using the Rossby number, the potential vorticity, and the Thomas angle (Thomas et al., 2013; Buckingham et al., 2021a).

We organize this work as follows: i) in Section 2 we describe our numerical setup and the methods to diagnose submesoscale instabilities and perform the energy analyses; ii) in Section 3 we investigate the submesoscale horizontal shear instabilities associated with the BC meanders; and iii) in Section 4 we summarize our results and draw our conclusions.

2 Methods

2.1 Numerical simulation

We perform a high-resolution numerical simulation using CROCO (Coastal Regional Oceanic COmmunity model; code available at `https://www.croco-ocean.org/`) in the hydrostatic mode. CROCO is built upon ROMS-AGRIF and solves the free surface, hydrostatic and primitive equations in terrain-following coordinates using a time-splitting implementation (Shchepetkin & McWilliams, 2005). We run the model between 50°W - 30°W and 28°S - 17°S (Figure 2.1), and use a horizontal resolution of 1/50° ($\sim 2\,km$) with 30 sigma levels (stretching parameters: $\theta_s = 6$, $\theta_b = 4$ and $h_c = 50$).

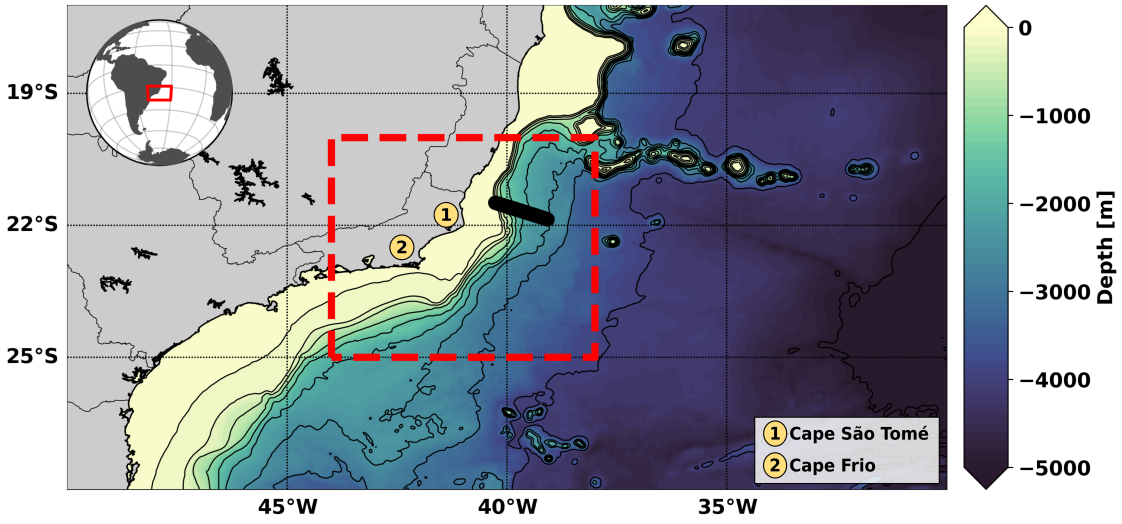

Figure 2.1: Model domain and filtered GEBCO2021 topography. The red dashed box and the black transect are areas used for the model evaluation (Appendix A).

The simulation initial and boundary conditions are from the 1/12° GLORYS12V1 daily reanalysis, and the model is forced by 6-hourly ERA5 atmospheric bulk fluxes and TPX07 tides. The model bathymetry is extracted from GEBCO2021 (available at `https://www.gebco.net/`), and filtered to limit the maximum $\frac{\nabla h}{h}$ to 0.25 in order to prevent horizontal pressure gradients errors that are common in terrain-following coordinate models (Haney, 1991). The simulation

spans from 2015 to 2019 and has one year of spin-up. Although the simulation is dated, we do not intend to reproduce specific events. Rather, we aim to simulate realistic events that capture the submesoscale dynamics associated with the BC meanders (check Appendix A to see the model evaluation).

We use a fifth-order upwind scheme for the horizontal advection of momentum and tracers, and fourth-order centered schemes for the vertical advection of momentum and tracers. Both high-order schemes are of higher accuracy and reduce spurious diapycnal mixing (Soufflet et al., 2016). We include vertical mixing in the simulation using the *K-profile parameterization* (KPP) in the interior ocean and within the surface and bottom boundary layers. On the other hand, numerical constraints control horizontal mixing as we solve the horizontal advection with an upwind scheme. For the fifth-order scheme, dissipation extends to wavelengths of $5\Delta x$ (submesoscale vortices with $5\,km$ diameters). Lastly, bottom friction is parameterized in the model using a linear function with a drag coefficient of $3 \times 10^{-4}\,\mathrm{m\,s^{-1}}$.

2.2 Potential Vorticity analysis

Assuming that $2\Omega = f\vec{k}$, the Ertel Potential Vorticity (q) is equal to:

$$q = \vec{\omega_a} \cdot \nabla b = \underbrace{(f+\zeta)N^2}_{q_{vert}} + \underbrace{\left(\frac{\partial u}{\partial z} - \frac{\partial w}{\partial x}\right)\frac{\partial b}{\partial y} + \left(\frac{\partial w}{\partial y} - \frac{\partial v}{\partial z}\right)\frac{\partial b}{\partial x}}_{q_{bc}}, \tag{2.1}$$

where ω_a is the absolute vorticity, N^2 is the stratification, q_{vert} is the vertical component of q, and q_{bc} is the baroclinic component of q.

A consequence of the Ertel Potential Vorticity theorem is that, in a baroclinic fluid, conservation of q implies conservation of buoyancy (e.g., Buckingham et al., 2021a). In the interior ocean, q is approximately conserved and the product fq is always positive. However, close to the boundaries where diabatic processes can occur due to the intensification of friction and buoyancy fluxes, q can be injected/extracted.

Injection of q in the bottom boundary layer occurs when the shear between a jet and topography increases cyclonic vorticity. In some occasions, q injection can lead to submesoscale barotropic shear instability (e.g., Gula et al., 2015, 2016a). Here, we use q along with Ro $(= \zeta/f)$

to find events where the BC might be developing barotropic shear instability.

Extraction of q in the bottom boundary layer occurs when the shear between a jet and topography increases anticyclonic vorticity. During this process, the product fq can become negative and submesoscale instabilities can be developed in thermal-wind balanced fronts (Thomas et al., 2013). If fq becomes negative due to $N^2 < 0$, the instability is named gravitational instability. If $fq < 0$ with $fq_{vert} < 0$ and $N^2 > 0$ in a barotropic flow, inertial instability occurs. Lastly, if $fq < 0$ with $fq_{bc} < 0$ and $fq_{vert} > 0$, symmetric instability occurs. Based on energy exchange rates for a thermal-wind balanced flow, Thomas et al. (2013) have shown that these different instability regimes can be differentiated by the following angles:

$$\phi_{tw} = tan^{-1}\left(-\frac{1}{Ri_B}\right) = tan^{-1}\left(-\frac{|\nabla_h b|^2}{f^2 N^2}\right), \tag{2.2}$$

$$\phi_{tw_c} = tan^{-1}\left(\frac{\zeta_g}{f}\right). \tag{2.3}$$

See the instability categories according to these angles in Table 2.1.

Table 2.1: Instability categories for thermal-wind balanced flows (TWB) according to ϕ_{tw} and ϕ_{tw_c} (Thomas et al., 2013), and instability categories for gradient-wind balanced flows (GWB) according to ϕ_{gw} and ϕ_{gw_c} (Buckingham et al., 2021a). Categories: Stable (St.), Symmetric (S), Inertial (I) and Gravitational (G).

	Thomas angle			
	TWB		**GWB**	
Inst.	**Cyclonic**	**Anticyclonic**	**Cyclonic**	**Anticyclonic**
St.	$\phi_{tw_c} < \phi_{tw} \leq 0$	$\phi_{tw_c} < \phi_{tw} \leq 0$	$\phi_{gw_c} < \phi_{gw} \leq 0$	$\phi_{gw_c} < \phi_{gw} \leq 0$
S+I	—	$-\frac{\pi}{4} < \phi_{tw} \leq \phi_{tw_c}$	—	$-\frac{\pi}{4} < \phi_{gw} \leq \phi_{gw_c}$
S	$-\frac{\pi}{2} < \phi_{tw} \leq \phi_{tw_c}$	$-\frac{\pi}{2} < \phi_{tw} \leq -\frac{\pi}{4}$	$-\frac{\pi}{2} < \phi_{gw} \leq \phi_{gw_c}$	$-\frac{\pi}{2} < \phi_{gw} \leq -\frac{\pi}{4}$
G+S	$-\frac{3\pi}{4} < \phi_{tw} \leq -\frac{\pi}{2}$	$-\frac{3\pi}{4} < \phi_{tw} \leq -\frac{\pi}{2}$	$-\frac{3\pi}{4} < \phi_{gw} \leq -\frac{\pi}{2}$	$-\frac{3\pi}{4} < \phi_{gw} \leq -\frac{\pi}{2}$
G	$-\pi < \phi_{tw} \leq -\frac{3\pi}{4}$	$-\pi < \phi_{tw} \leq -\frac{3\pi}{4}$	$-\pi < \phi_{gw} \leq -\frac{3\pi}{4}$	$-\pi < \phi_{gw} \leq -\frac{3\pi}{4}$

Although very useful, the $fq < 0$ criterion does not yield a generalized sufficient criterion for submesoscale instabilities. The sufficient criterion arises when centrifugal effects are taken into account (gradient-wind balanced flows). Buckingham et al. (2021a) and Buckingham et al. (2021b) have shown that the product of Ertel's potential vorticity and absolute angular momen-

tum must be positive in an inviscid front for stability. Instability occurs if:

$$(1 + Cu)fq < 0, \tag{2.4}$$

where Cu (Curvature number) is equal to:

$$Cu = \frac{2\,|\vec{v}|}{fr}, \tag{2.5}$$

and r is the local radius of curvature (Theisel & Rauschenbach, 1999):

$$r = \frac{\left(u^2 + v^2\right)^{3/2}}{u^2 \frac{\partial v}{\partial x} - v^2 \frac{\partial u}{\partial y} + uv\left(\frac{\partial v}{\partial y} - \frac{\partial u}{\partial x}\right)}. \tag{2.6}$$

Equation 2.4 is the generalized Rayleigh criterion Buckingham et al. (2021a,b). This criterion shows that an exchange of vorticity, stratification, and centripetal accelerations must happen so that stability can be attained (Buckingham, 2021). Note that it reduces to the criterion originally used for thermal wind balanced fronts ($fq < 0$) when centrifugal effects are negligible ($Cu \to 0$; $r \to \infty$).

Based on the non-dimensional product of the Ertel Potential Vorticity and the absolute angular momentum, Buckingham et al. (2021a) modified the instability angles introduced by Thomas et al. (2013):

$$\phi_{tw} \to \phi_{gw} = tan^{-1}\left(-\frac{(1 + Cu)^2}{Ri}\right), \tag{2.7}$$

$$\phi_{tw_c} \to \phi_{gw_c} = tan^{-1}\left(-(1 + Cu)(1 + Ro)\right). \tag{2.8}$$

where $Ri = N^2/\left|\partial v/\partial z\right|^2$. See the instability categories according to ϕ_{gw} and ϕ_{gw_c} in Table 2.1. This instability classification shows what aspect of the flow is most responsible for reducing the $(1+Cu)fq$ discriminant, but it should not be interpreted in terms of energy exchange under linear instability as the classification from Thomas et al. (2013). In this work, we use the $(1+Cu)fq < 0$ criterion and the gradient wind Thomas angle (ϕ_{gw}) to investigate the occurrence of symmetric and inertial instabilities associated to the interaction of the BC meanders with topography.

2.3 Energy conversions

As shown in the last section, when $(1+Cu)fq$ becomes negative, symmetric, inertial, and gravitational instabilities can arise. However, some submesoscale instabilities, such as barotropic shear instability (e.g., Gula et al., 2015, 2016a), can occur even when the product $(1+Cu)fq$ is positive. Since the Thomas angle does not capture this positive $(1+Cu)fq$ instability, we analyze energy conversions to investigate the occurrence of barotropic shear instability.

Baroclinic instability plays an important role in the BC meanders dynamics. According to Silveira et al. (2008) and Rocha et al. (2014), off CST and CF, the BC meanders grow quasi-stationarily through baroclinic instability. Thus, we take advantage of the energy conversions analysis and also assess the occurrence of baroclinic instability during the BC meander's growth.

From the Eddy Kinetic Energy (EKE) and the Eddy Potential Energy (EPE) conservation equations (see Chen et al., 2014; Magalhães et al., 2017; Napolitano et al., 2019) we analyze three terms: 1) the Horizontal Shear Production (HSP); 2) the Buoyancy Production (BP), and; 3) the Buoyancy Flux (BF). See the expressions below:

$$\underbrace{HSP = -\overline{u'^2}\frac{\partial \overline{u}}{\partial x} - \overline{u'v'}\frac{\partial \overline{u}}{\partial y} - \overline{v'^2}\frac{\partial \overline{v}}{\partial y} - \overline{u'v'}\frac{\partial \overline{v}}{\partial x}}_{MKE \rightarrow EKE}, \tag{2.9}$$

$$\underbrace{BP = -\left(\frac{1}{N^2}\right)\left[\overline{u'b'}\frac{\partial \overline{b}}{\partial x} + \overline{v'b'}\frac{\partial \overline{b}}{\partial y} + \overline{w'b'}\frac{\partial \overline{b}}{\partial z}\right]}_{MPE \rightarrow EPE}, \tag{2.10}$$

$$\underbrace{BF = -\overline{w'b'}}_{EPE \rightarrow EKE}. \tag{2.11}$$

The overbars denote time averages, and the primes the deviations from that average. We adopt 7-day means to investigate the occurrence of instabilities during the generation and growth of the mesoscale cyclones.

The HSP term shows the transfer of energy from the Mean Kinetic Energy (MKE) to the EKE (Chen et al., 2014). Negative HSP denotes the pathway $EKE \rightarrow MKE$ while positive HSP denotes $MKE \rightarrow EKE$ which occurs through horizontal shear instabilities. The BP term shows the transfer of energy from the Mean Potential Energy (MPE) to the EPE, while the BF term shows transfers from EPE to EKE (Chen et al., 2014). Analogously to the HSP,

negative BP (BF) means a $EPE \rightarrow MPE$ ($EKE \rightarrow EPE$) transfer, while positive BP (BF) means a $MPE \rightarrow EPE$ ($EPE \rightarrow EKE$) transfer. If both BP and BF are positive, we have a telltale signal of baroclinic instability (Pedlosky et al., 1987).

2.4 Kinetic Energy Flux across scales

Kinetic Energy (KE) fluxes across scales through nonlinear interactions. Traditionally, KE fluxes are measured using spectral methods. However, these methods rely upon the assumption of statistical homogeneity or a large-scale separation between the eddying scales of motion and the scales over which the statistics vary (e.g., Aluie et al., 2018). By contrast, the so-called "coarse-graining" approach is capable of quantifying kinetic energy fluxes across scales in any geographic location and any instant of time, without relying on assumptions of homogeneity or isotropy (e.g., Aluie et al., 2018; Schubert et al., 2020, 2021). Here, we use this method to quantify the kinetic energy fluxes between submesoscale motions and larger scale flows.

The method is applied as follows. For a scalar field, such as the zonal velocity component, we obtain a low-pass filtered field by applying the convolution

$$\overline{u(x,y)} = C \times u(x,y), \tag{2.12}$$

where C is a normalized window function, and $\overline{u(x,y)}$ is a low-pass filtered field which only contains scales larger than L. Following Aluie et al. (2018), we choose C to be the top-hat kernel:

$$C(\vec{R}) = \begin{cases} 1/A, & if \quad \left|\vec{R}\right| < L/2 \\ 0 & otherwise, \end{cases} \tag{2.13}$$

where $A = \pi L^2/4$ is the normalization area with diameter L, and $\vec{R}$ is the radial position vector.

We apply this convolution to all the velocity components and obtain the low-passed filtered fields $\overline{\vec{u}} = (\overline{u}, \overline{v}, \overline{w})$. The equations of motion do not change their form when we apply this convolution (Aluie et al., 2018). There is only one new term that arises from the nonlinear

advection term:

$$\nabla \cdot \overline{\vec{u}\vec{u}} = \nabla \cdot \overline{\vec{u}}\,\overline{\vec{u}} + \nabla \cdot \overline{\tau}\left(\vec{u},\vec{u}\right). \tag{2.14}$$

where $\overline{\tau}\left(\vec{u},\vec{u}\right) = \overline{\vec{u}\vec{u}} + \overline{\vec{u}}\,\overline{\vec{u}}$ is called the subfilter stress tensor that consists on the force that the unfiltered motions exert on the low-pass filtered flow.

To obtain the Kinetic Energy Flux expression, we need to compute the large-scale kinetic energy budget. This is done by multiplying the momentum equations by $\rho_0\overline{\vec{u}}$. When multiplying the subfilter stress by $\rho_0\overline{\vec{u}}$, we obtain:

$$\rho_0\overline{\vec{u}} \cdot \left[\overline{\tau}\left(\vec{u},\vec{u}\right)\right] = \nabla \cdot \left[\rho_0\overline{\vec{u}}\overline{\tau}\left(\vec{u},\vec{u}\right)\right] + \Pi. \tag{2.15}$$

The first term on the right-hand side is the divergence of the transport of large-scale kinetic energy by small-scale currents, while the second term is the kinetic energy flux across scales (Π):

$$\Pi = -\rho_0\left[\left(\overline{u^2} - \overline{u}^2\right)\overline{\frac{\partial u}{\partial x}} + \left(\overline{uv} - \overline{u}\,\overline{v}\right)\left(\overline{\frac{\partial u}{\partial y}} + \overline{\frac{\partial u}{\partial x}} + \left(\overline{v^2} - \overline{v}^2\right)\overline{\frac{\partial v}{\partial y}}\right)\right], \tag{2.16}$$

where negative (positive) values denote upscale (downscale) Kinetic Energy fluxes. Here, we compute Π to check if a submesoscale-to-mesoscale inverse cascade contributes to the growth of the BC mesoscale meanders as in the California Undercurrent case (Molemaker et al., 2015). We use the coarse-graining algorithm from Schubert & Rath (2021) to perform these computations. As the first internal Rossby radius of deformation is ~ 25 km in the region (Houry et al., 1987), we adopt L=50 km as the transition scale between submesoscale and mesoscale flows.

3 Results and Discussion

3.1 Brazil Current meanders formation

To analyze the occurrence of horizontal shear instabilities associated with BC meanders, we use a CST cyclone event that starts in September 2016 of the CROCO simulation. We observe that the CST cyclone is generated after an impinging anticyclone reaches the continental slope coming from the east (Figure 3.1a-c). This event displays a typical configuration of upstream-anticyclone and downstream-cyclone that was also observed in summer and in fall by Mill et al. (2015) and Pereira et al. (2019), respectively. Furthermore, altimetry observations confirm that both CST and CF cyclones can be generated after incoming anticyclones reach the continental slope. For instance, Figure 3.2 displays horizontal distributions of stream function (ψ) and geostrophic velocities ($\vec{u_g}$) data from the Sea Level Thematic Center (SL-TAC; distributed by CMEMS) during the formation of CST and CF eddies in 2008 and 2018, respectively.

In CROCO's simulation, we observe that, when the incoming anticyclone of September 2016 reaches the continental slope upstream of 22.15°S, the cyclonic vorticity increases and Ro reaches $\mathcal{O}(1)$ values in the region (Figure 3.3a). The CST cyclone is generated subsequently, when the amplified cyclonic vorticity is shed to the ocean interior (Figure 3.3b). The anticyclone keeps interacting with the slope and ejects strong cyclonic filaments that feed the CST eddy and contribute to its growth. By 8 October 2016, we observe a submesoscale cyclone and a belt of intense vorticity inside the mesoscale meander (Figure 3.3c). Eventually, a second submesoscale cyclone is formed and additionally contributes to the CST cyclone growth (Figure 3.3d). Figure 3.4a shows the isopycnal and velocity structure of the meso- and submesoscale cyclones (blue transect from Figure 3.3d). The two submesoscale cyclones span the upper 600 m and have radii of ~20 km. They present associated $\mathcal{O}(1)$ Rossby numbers and generate 50-100 $\mathrm{m\,d^{-1}}$ vertical velocities, but the associated Richardson number does not reach $\mathcal{O}(1)$ values (Figures 3.4b-d).

In April 2018, we observe a similar CF cyclone event generation: i) anticyclone arrival and vorticity amplification upstream (Figures 3.1d-e and 3.3e); ii) mesoscale cyclone formation downstream (Figures 3.1f and 3.3f) and; iii) ejection of filaments and formation of a submesoscale

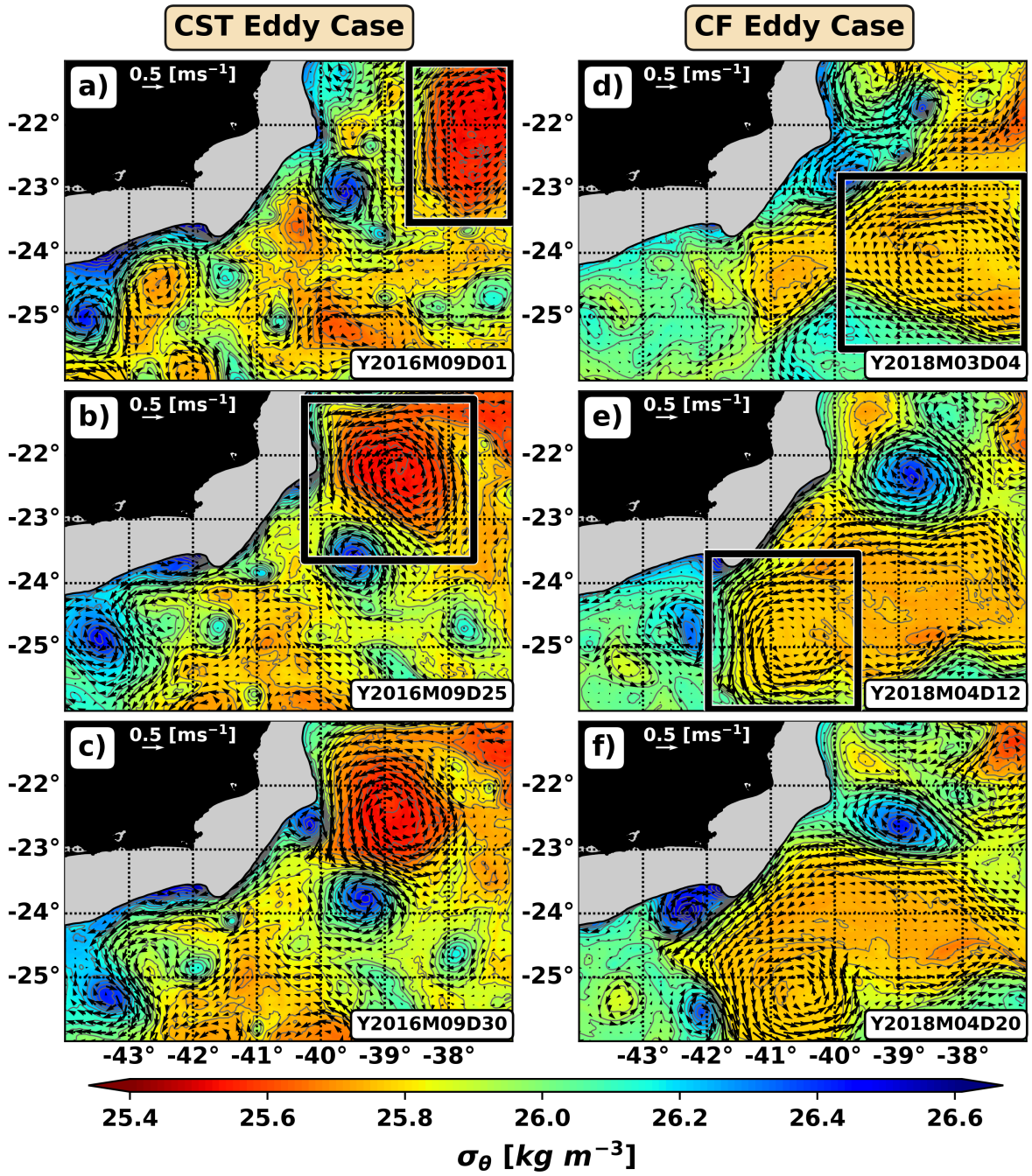

Figure 3.1: Horizontal distributions of σ_θ at $160\,m$ in: a) September 1^{st} 2016; b) September 25^{th} 2016; c) September 30^{th} 2016; d) March 3^{rd} 2018; e) April 4^{th} 2018, and; f) April 20^{th} 2018. Black solid boxes track the incoming anticyclones before the formation of the CST and CF cyclone events.

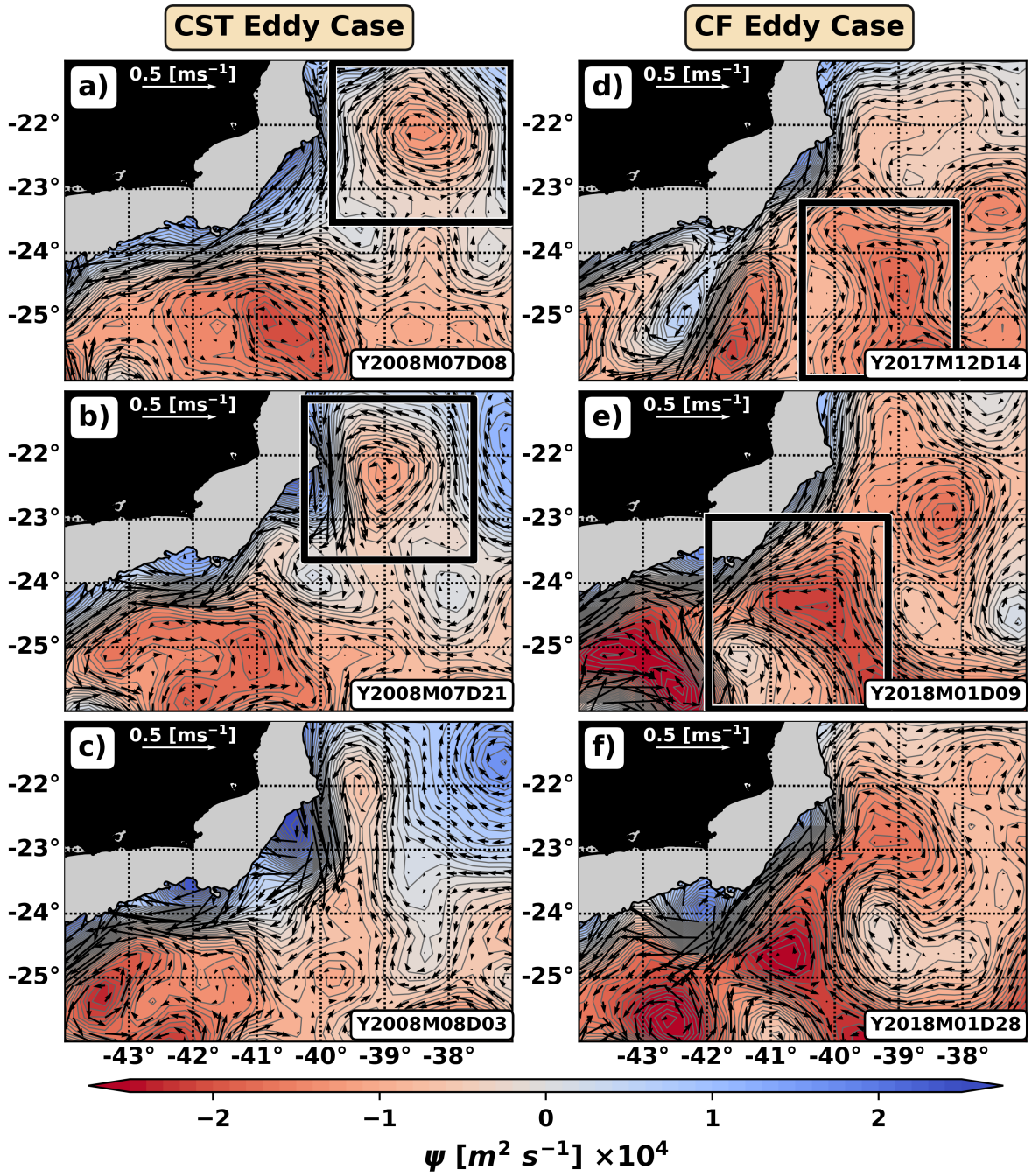

Figure 3.2: Horizontal distributions of ψ and $\vec{u_g}$ derived from altimetry observations in: a) 8 July 2008; b) 21 July 2008; c) 3 August 2008; d) 14 December 2017; e) 9 January 2018, and; f) 28 January 2018. Black solid boxes track the incoming anticyclones before the formation of the CST and CF cyclone events.

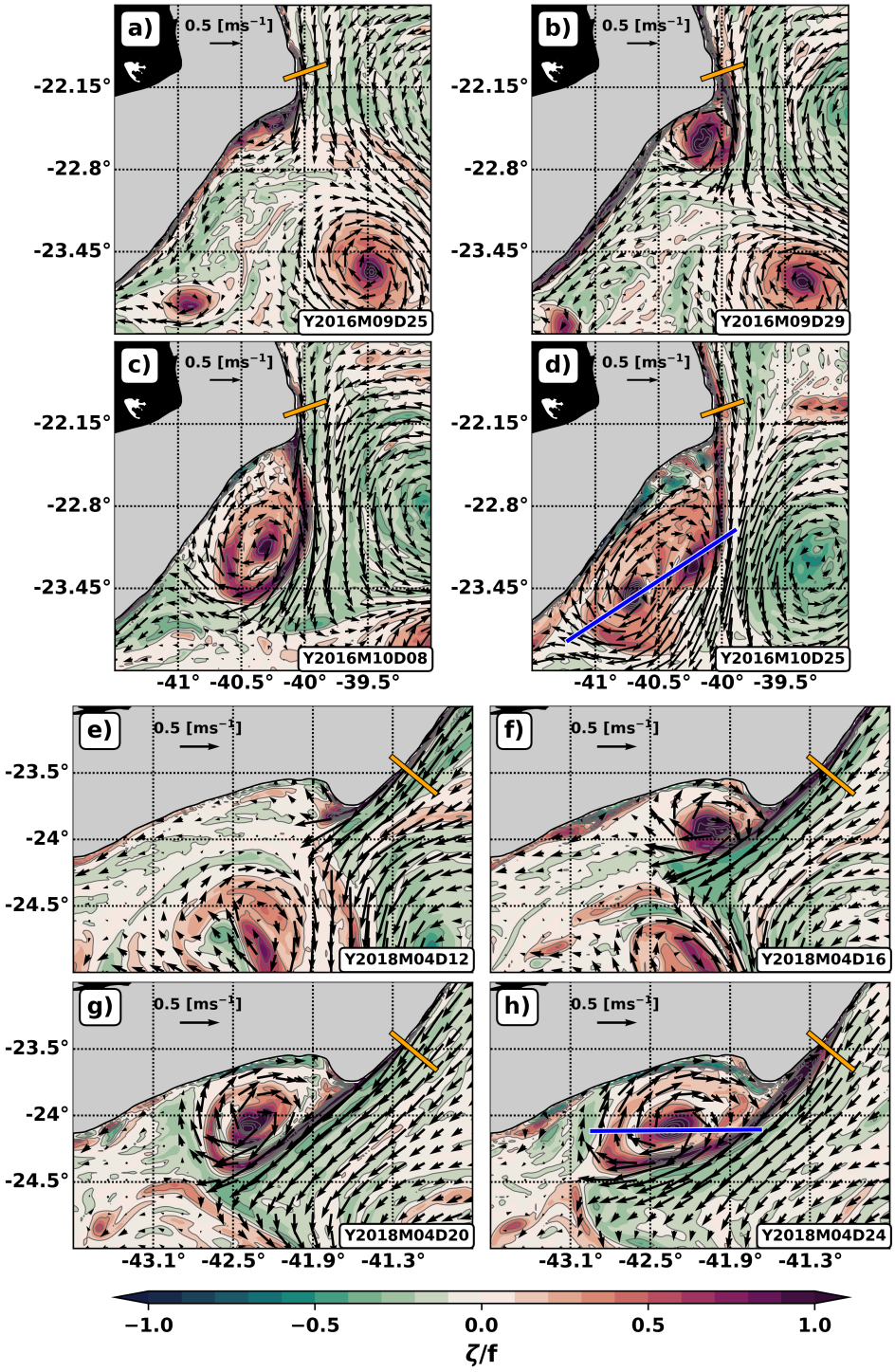

Figure 3.3: Horizontal distributions of ζ/f at $160\,m$ during a CST cyclone event in September-October 2016 (a-d) and a CF cyclone event in April 2018 (e-h).

cyclone (Figures 3.3g-h). As in the CST event, in Figures 3.4e-h we observe a clear signature of a submesoscale cyclone with ∼20 km of radius on the vertical sections (blue transect from Figure 3.3h) of cross-section velocity, Rossby number and vertical velocity. Furthermore, this submesoscale cyclone spans from 600 m to 50 m and, once again, the Richardson number does not reach $\mathcal{O}(1)$ values within it (Figure 3.4g).

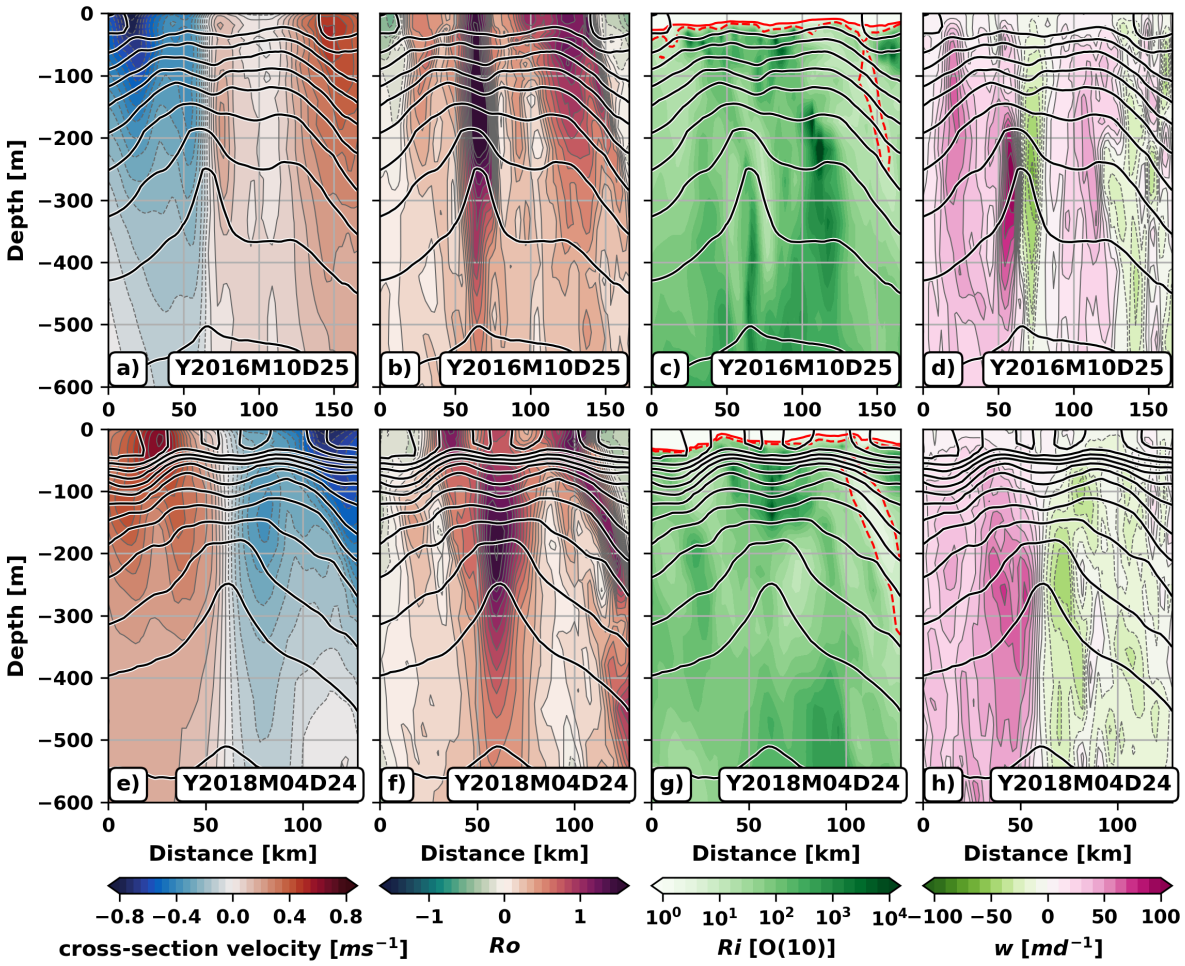

Figure 3.4: Vertical sections of the cross-section velocities (1^{st} column), the Rossby number (2^{nd} column), the Richardson number (3^{rd} column), and the vertical velocities (4^{th} column) at the blue transect from Figure 3.3d (1^{st} row) and Figure 3.3h (2^{nd} row). Black solid contours show isopycnals. Red solid and dashed contours on panels c and g show the lower and upper limits, respectively, of $\mathcal{O}(1)$ Richardson number.

The amplification of the cyclonic vorticity ($Ro \sim 2$) adjacent to the bottom boundary spans, approximately, from 100 m to 400 m in both events (Figures 3.5a-h). Consequently, fq is injected

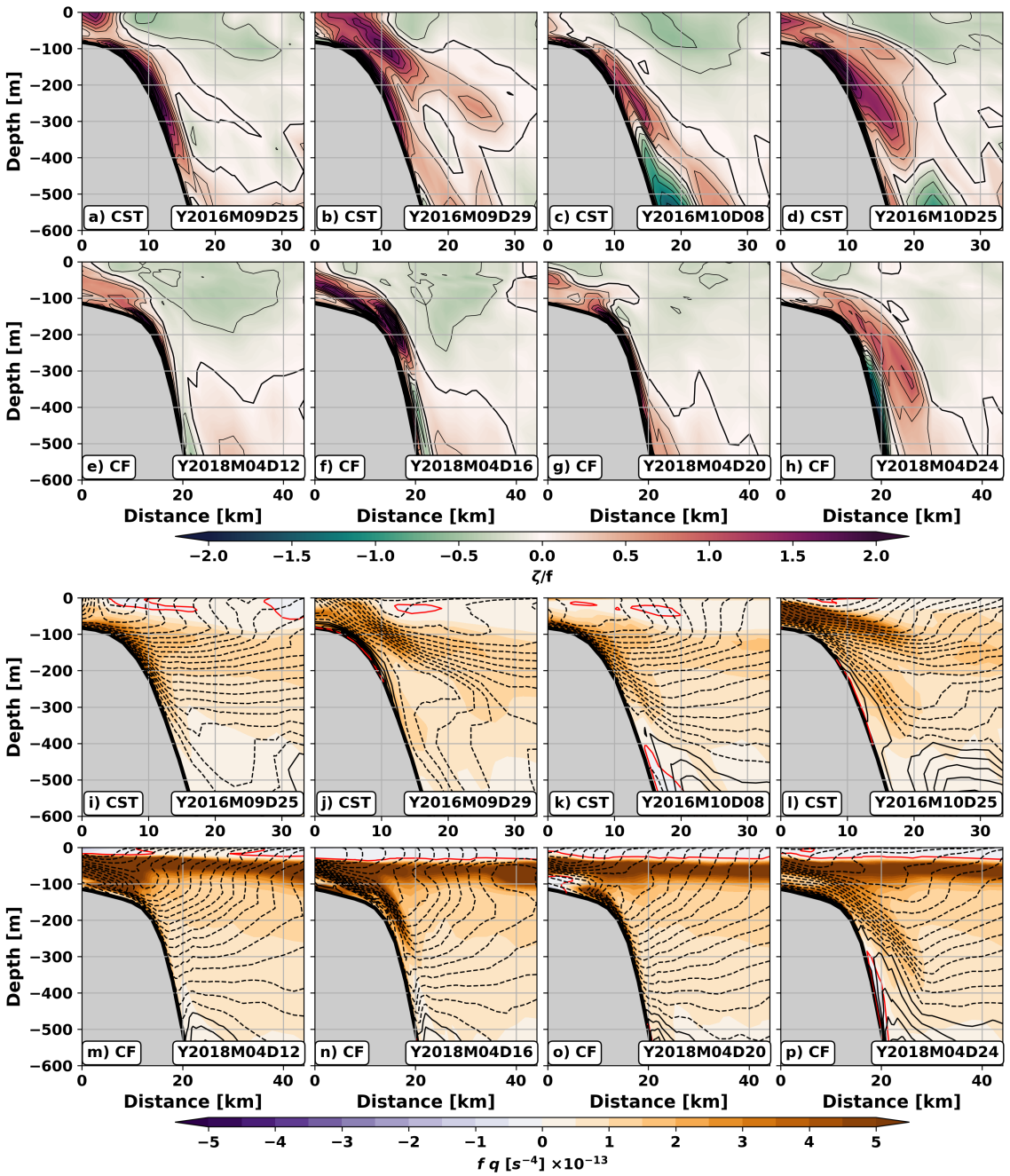

Figure 3.5: Vertical sections of ζ/f at the orange transects from Figure 3.3 during the CST cyclone event (panels a-d), and the CF cyclone event (panels e-h). Similarly, vertical sections of fq during the CST cyclone event (panels i-l) and the CF cyclone event (panels m-p). Isotachs are shown on panels i-p, with positive (negative) values represented by solid (dashed) isolines. Red isolines show $fq = 0$ contours.

near the bottom exceeding $5\times10^{-13}s^{-4}$ values (Figures 3.5i-p). Note that the amplification of both properties occurs where the anticyclone squeezes the BC against the slope and, consequently, increases the shear (Figures 3.5i-p).

We perform an energy analysis to verify if barotropic shear instability is involved in this process. Our results show that the vertically integrated HSP (100 m - 300 m) is positive where the incoming anticyclone interacts with the slope (Figures 3.6a-c). Thus, similarly to the Gulf Stream case (Gula et al., 2016a), barotropic shear instability indeed plays a role in the formation of BC meanders. Furthermore, it also ejects filaments and submesoscale cyclones that contribute to the meanders' growth. This explains why the submesoscale cyclones do not reach $O(1)$ Ri. Their generation through barotropic shear instability does not involve a reduction of the stratification.

Downstream, the BP and BF terms are concomitantly positive in some regions within the mesoscale cyclones (Figures 3.6d-i). Thus, in accordance with Silveira et al. (2008), Rocha et al. (2014) and Magalhães et al. (2017), our analysis shows that baroclinic instability occurs during the growth of the BC meanders. We show that, although prone to baroclinic instability from 20°S to 36°S (Magalhães et al., 2017), conditions for the development of recurrent baroclinically-unstable BC cyclones are perfect off CST and CF because of: i) the arrival of mesoscale anticyclones upstream of separation regions, and; ii) the subsequent generation of submesoscale barotropic shear instability that triggers the BC meanders formation.

We applied the same energy analysis to a CST cyclone event from a 0.1° horizontal resolution OfES simulation (Appendix B). In this lower-resolution simulation, the process occurs similarly, but through balanced dynamics (e.g., Molemaker et al., 2015). The cyclones are still triggered by barotropic instability, and baroclinic instability contributes to their growth. However, when the submesoscale dynamics is not taken into account, energy conversions are approximately two orders of magnitude smaller. In a model sensitivity experiment, Santana et al. (2020) showed that downscaling from a 1/4° to a 1/24° horizontal resolution model: i) improves the representation of observed CST eddies in operational models, and; ii) increases the simulated energetic levels in the studied regions. We speculate that the representation of the submesoscale dynamics in their higher resolution simulation played a key role to improve the CST eddies predictability.

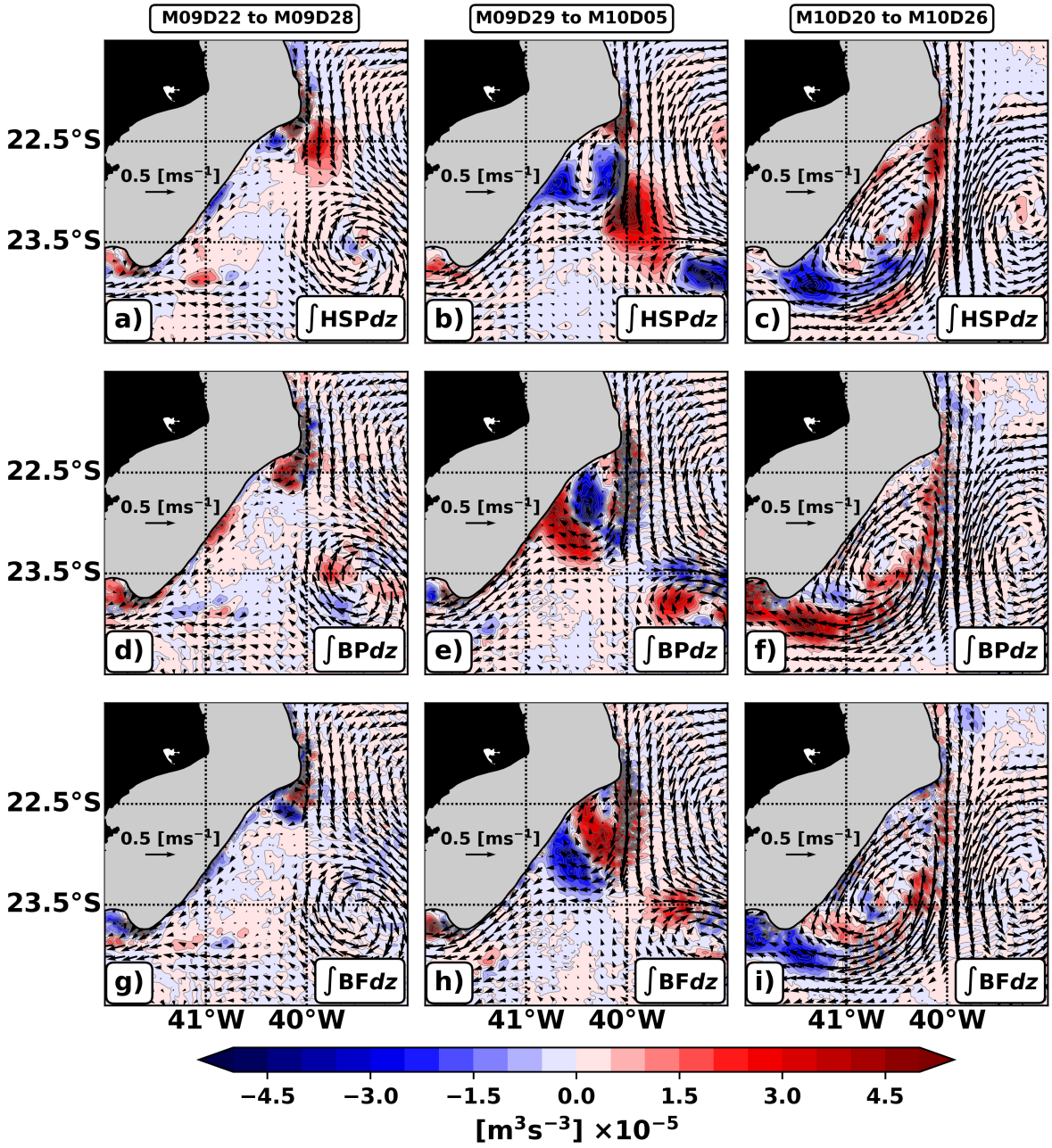

Figure 3.6: Energy analysis for the CST cyclone 2016 event shown on Figures 3.3a-d. Horizontal distributions of the vertically-integrated (100 m to 300 m) HSP (1^{st} row), BP (2^{nd} row), and BF (3^{rd} row). The 1^{st} column shows the period between September 22 to 28, the 2^{nd} column the period between September 29 to October 5, and the 3^{rd} column the period between October 20 to October 26.

3.2 The submesoscale-to-mesoscale inverse cascade

In the last section, we have shown that submesoscale barotropic shear instability is responsible to trigger the formation of BC meanders. In addition, we have shown that this instability sheds cyclonic filaments and submesoscale cyclones that feed the mesoscale meanders. In this section, we aim to answer if these submesoscale features contribute to the growth of the meanders in a submesoscale-to-mesoscale inverse cascade.

To accomplish that, we analyze the Kinetic Energy Flux across scales using a coarse-graining approach (Aluie et al., 2018; Schubert et al., 2020, 2021). According to Houry et al. (1987), the first internal Rossby radius of deformation is ~ 25 km in the region. Thus, we adopt $L = 50\,\mathrm{km}$ as the transition scale between submesoscale and mesoscale flows. Figure 3.7 shows the KE fluxes through $L = 50\,km$ at $160\,m$ in the same CST cyclone event displayed in Figures 3.3a-d.

We observe that, after the formation of the CST cyclone, the KE fluxes are predominantly upscale inside the mesoscale meander (Figure 3.7). The most intense values ($\sim -1 \times 10^{-3}\,\mathrm{mW\,m^{-2}\,km^{-1}}$) are observed in October 25^{th} 2016 when there are two submesoscale cyclones within the eddy (Figures 3.3d and 3.7d). Indeed, the submesoscale features shed by barotropic shear instability contribute to the growth of the BC meanders in a submesoscale-to-mesoscale inverse cascade. This is similar to the California Undercurrent case, where inertial instability sheds filaments and Submesoscale Coherent Vortices (SCVs) that contribute to the growth of anticyclones downstream of a separation region (Molemaker et al., 2015).

The only region where KE fluxes are predominantly downscale is where the CST cyclone interacts with the slope (Figure 3.7d). This is a region where the shear between the eddy and the slope increases anticyclonic vorticity and leads Ro to $\mathcal{O}(1)$ values (Figure 3.3d). When anticyclonic vorticity is increased, $(1+Cu)fq$ can become negative and lead to inertially/symmetrically unstable flows. These instabilities contribute to the forward cascade of energy (Gula et al., 2016b), which is in accordance with the downscale KE fluxes found in the region. In the next section, we address the occurrence of these instabilities and their association with the generation of anticyclonic SCVs.

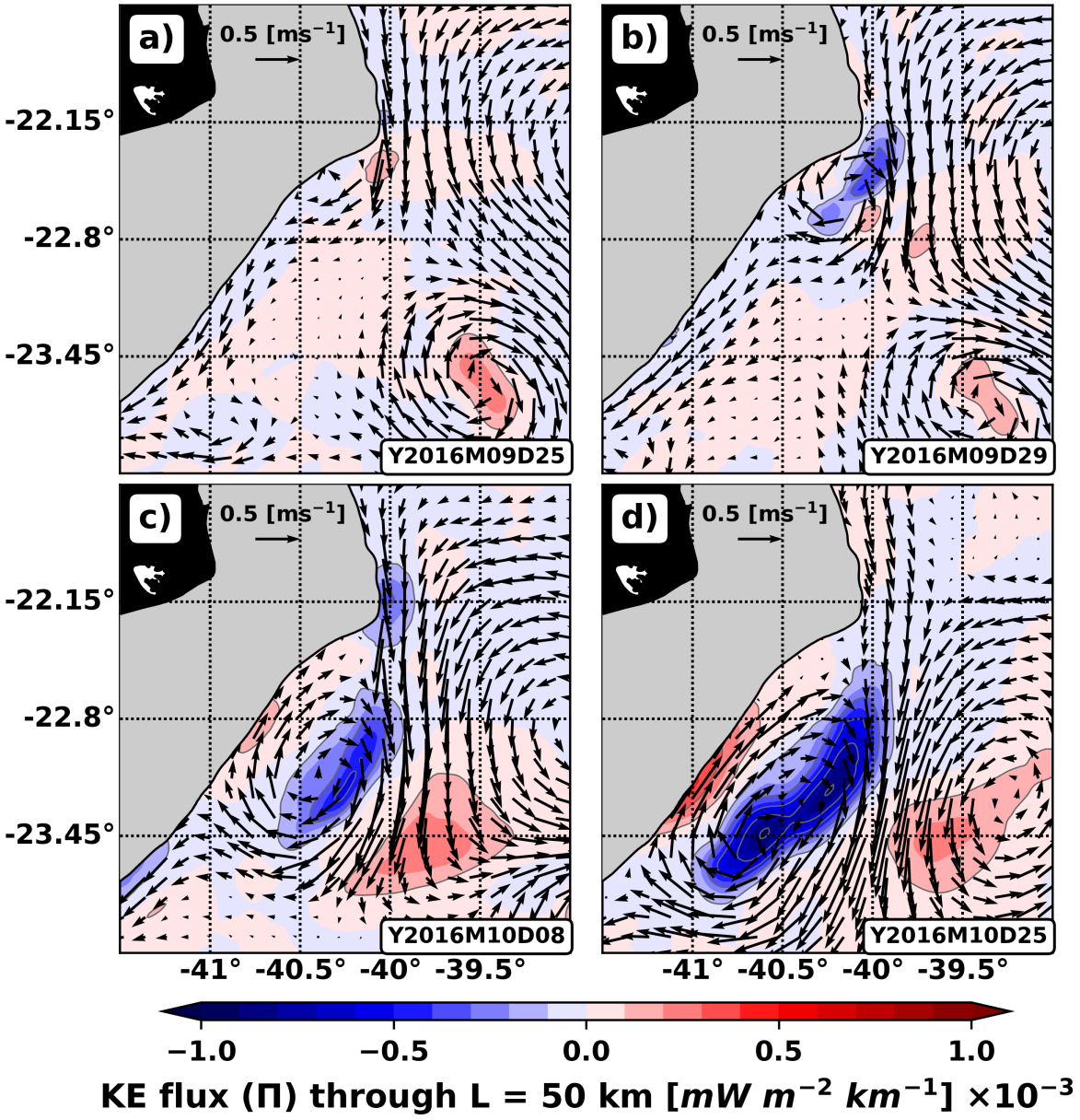

Figure 3.7: Horizontal distributions of Kinetic Energy flux through $L = 50\,km$ at 160 m during a CST cyclone event.

3.3 Submesoscale anticyclones generation

After the formation of the BC meanders, they grow quasi-stationarily adjacent to the shelf-break (Silveira et al., 2008). In the last sections, we have shown that during this process, the shear between the cyclones and the topography increases anticyclonic vorticity and generates downscale KE fluxes. In this section, we aim to answer if this process is associated with the development of inertial/symmetric instabilities and, subsequently, with the generation of anticyclonic SCVs (e.g., Molemaker et al., 2015; Morvan et al., 2019; Napolitano et al., 2021b; Lazaneo et al., 2022).

We start by analyzing the temporal evolution of Ro on a CST cyclone event at 450 m (March 2019). As in the cases mentioned before, we observe that the shear between the inshore limb of the mesoscale meander and the slope amplifies anticyclonic vorticity, and leads the Rossby number to $\mathcal{O}(1)$ values (Figure 3.8a). After some days, we observe that filaments of amplified anticyclonic vorticity are ejected offshore and roll-up into anticyclonic SCVs (Figures 3.8b and 3.8d). One of the generated SCVs is advected southward and orbit the whole periphery of the mesoscale meander until reaching the slope (Figures 3.8b-f), while the other is advected northward (Figures 3.8d-e).

Next, we address the stability of the flow during the SCVs generation process. In the region where the filaments are ejected and within the SCVs, the Curvature number ranges from -0.3 to -1.0 values (Figure 3.9). Thus, centrifugal effects must be considered to verify the stability of the flow. Indeed, the flow is unstable ($(1+Cu)fq < 0$) in the region where anticyclonic vorticity is amplified, and within the SCVs for some days (Figure 3.10). Figure 3.11a-c shows that the shear between the CST cyclone and the slope generates a region of negative $(1+Cu)fq$, $\mathcal{O}(1)$ Rossby number, and $\mathcal{O}(1)$ Richardson number between 100 m and 900 m. According to the gradient wind Thomas angle (Buckingham et al., 2021a), the flow is symmetrically and inertially unstable in this area (Figure 3.11d). The anticyclonic SCV that migrates south spans from 100 m to 700 m with radii between 10 and 15 km (Figures 3.11e-l). It remains symmetrically and inertially unstable for some days after its generation (Figures 3.11e-h). After that, it becomes marginally stable but still retain its convex-lens-shaped isopycnals and its $\mathcal{O}(1)$ Rossby number values (Figures 3.11i-l). Corroborating Wenegrat et al. (2018), we observe that a mix of inertial and symmetric instability occurs where topography is sharply sloped whereas symmetric instability

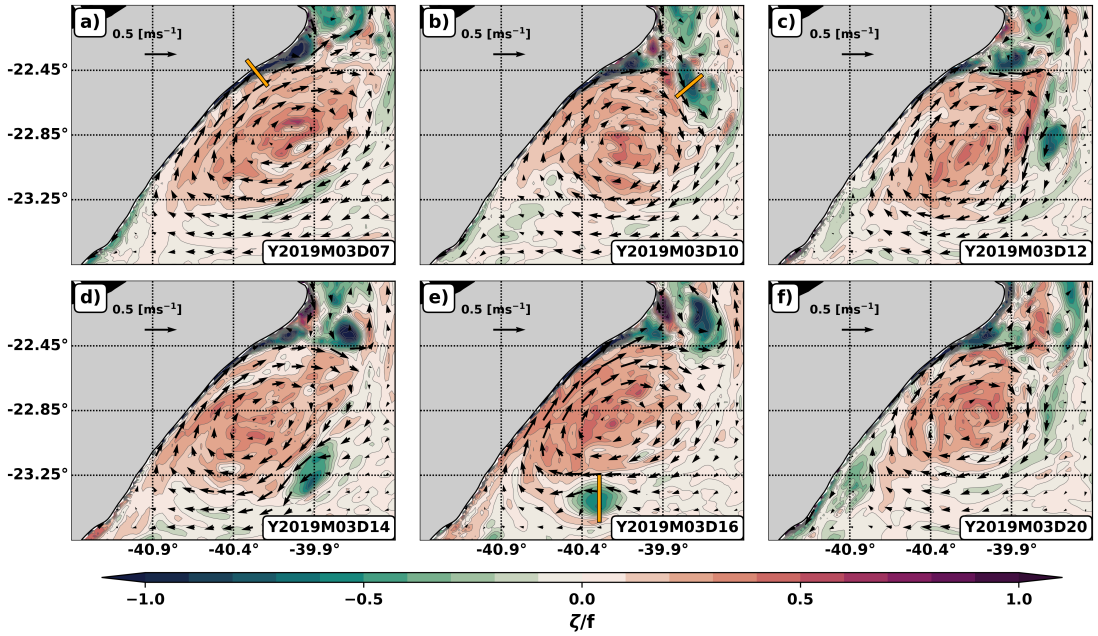

Figure 3.8: Horizontal distributions of ζ/f at $450\,m$ during a CST cyclone event in March 2019.

occurs where the sloped topography flattens.

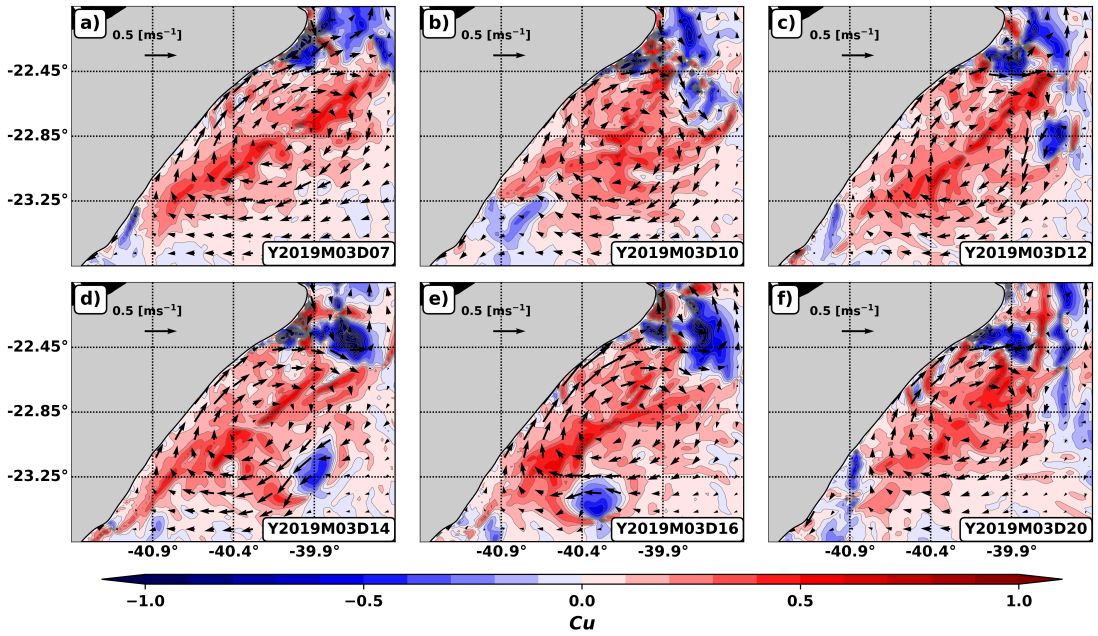

Figure 3.9: Horizontal distributions of Cu at $450\,m$ during a CST cyclone event in March 2019.

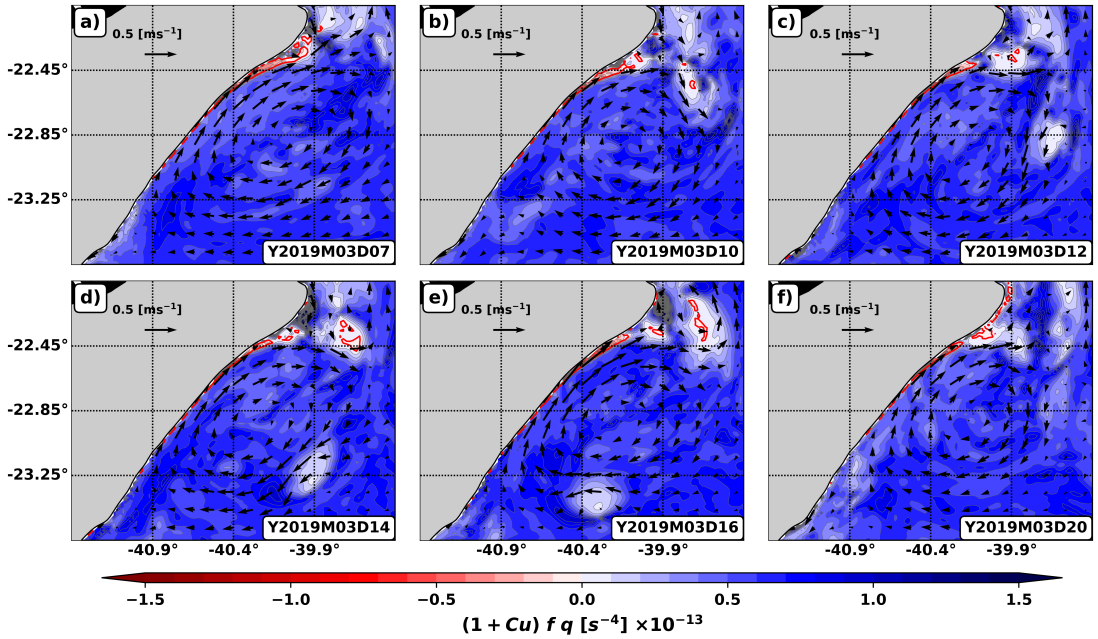

Figure 3.10: Horizontal distributions of $(1 + Cu)fq$ at $450\,m$ during a CST cyclone event in March 2019. Red solid lines show $(1 + Cu)fq = 0$ contours.

The southward migrating SCV is rapidly destroyed since it hits the continental slope. By contrast, the northward migrating SCVs can trigger the formation of subsurface mesoscale anticyclones (Figure 3.12). In particular, we observe this process occurring during an event of northward migration of the CST eddy in April 2019. Such migrating events were described by Mill et al. (2015), who estimated that approximately 20% of the CST cyclones translate north. Figures 3.12a-b and 3.12d-e show the northward migrating SCV from Figure 3.8e being advected at 450 m and keeping its low $(1 + Cu)fq$ signature. However, as the CST cyclone starts to migrate north, the interaction with the slope generates a second strong and unstable anticyclonic SCV that cascades $\sim 0.25\,\mathrm{mW\,m^{-2}\,km^{-1}}$ of KE downscale through $L = 50\,\mathrm{km}$ (Figures 3.12b, 3.12e and 3.12h). Subsequently, this SCV grows into a subsurface mesoscale anticyclone with a radius of $\sim 30\,\mathrm{km}$ (Figures 3.12c and 3.13a). This anticyclone presents associated $\mathcal{O}(1)$ Ro and Ri numbers (Figures 3.12c and 3.13b-c), as well as regions of flow instability (Figures 3.12f and 3.13d). Finally, we observe that KE is fluxed both up- and downscale inside the mesoscale anticyclone (Figure 3.12i). This occurs because the submesoscale features inside the eddy contribute to: i) the inverse cascade of energy by playing a role on the growth of the anticyclone, and; ii) the forward cascade of energy due to the instability of the flow.

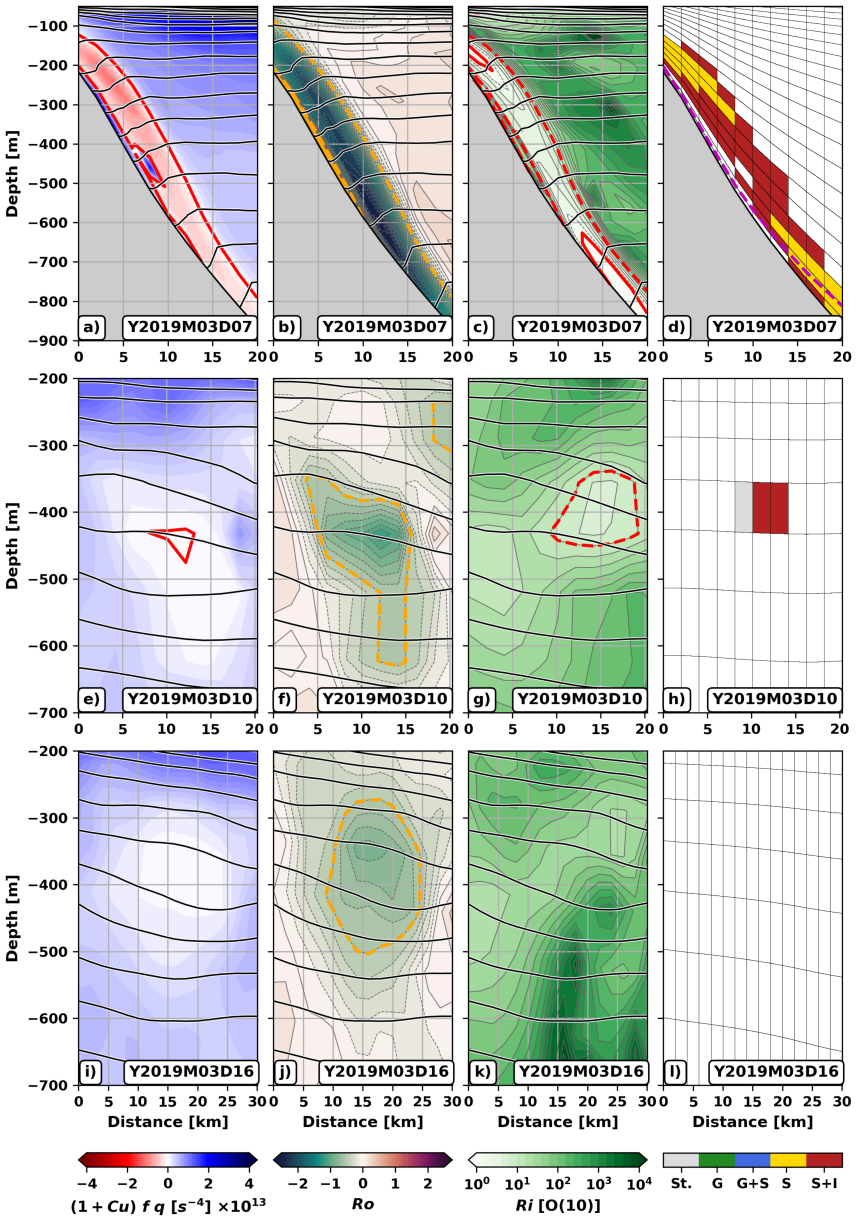

Figure 3.11: Vertical sections of $(1 + Cu)fq$ (1^{st} column), the Rossby number (2^{nd} column), the Richardson number (3^{rd} column), and the instability category (4^{th} column) at the yellow transect from: (1^{st} row) Figure 3.8a; (2^{nd} row) Figure 3.8b and; (3^{rd} row) Figure 3.8e. Black solid contours show isopycnals. Red solid contours on the 1^{st} column show the $(1 + Cu)fq = 0$ contour. Yellow dashed contours on the 2^{nd} column show the $Ro = -0.5$ contour. Red solid and dashed contours on the 3^{rd} column show the lower and upper limits, respectively, of $\mathcal{O}(1)$ Richardson number.

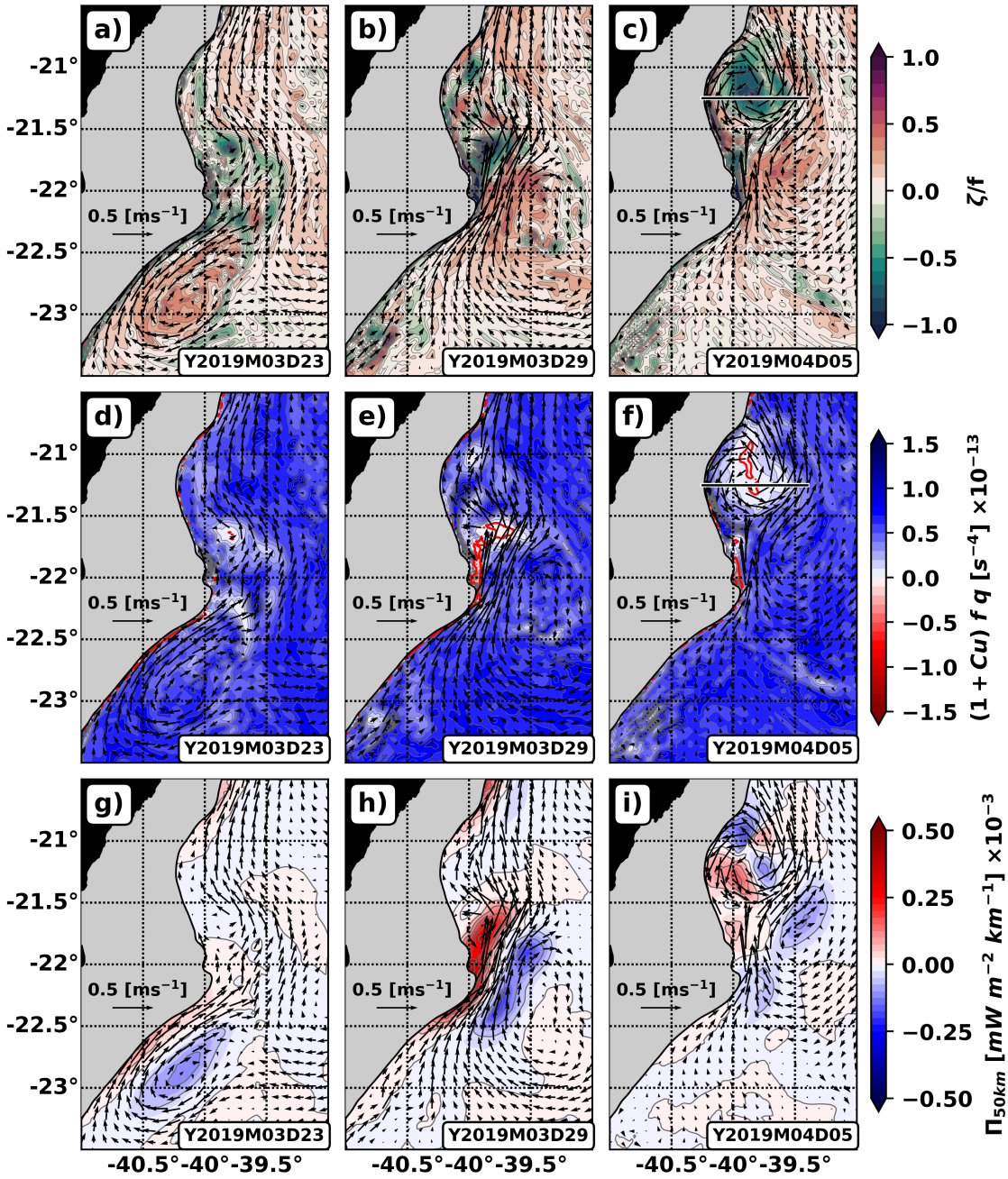

Figure 3.12: Northward migration CST cyclone event observed at 450 m in March-April 2019. Horizontal distributions of: (1^{st} row) ζ/f; (2^{nd} row) $(1+Cu)fq$, and; (3^{rd} row) Kinetic Energy flux through $L = 50\,km$. The red solid isolines on the 2^{nd} row show $(1+Cu)fq = 0$ contours, and the black solid line on panels c and f show a transect crossing the mesoscale anticyclone (Figure 3.13).

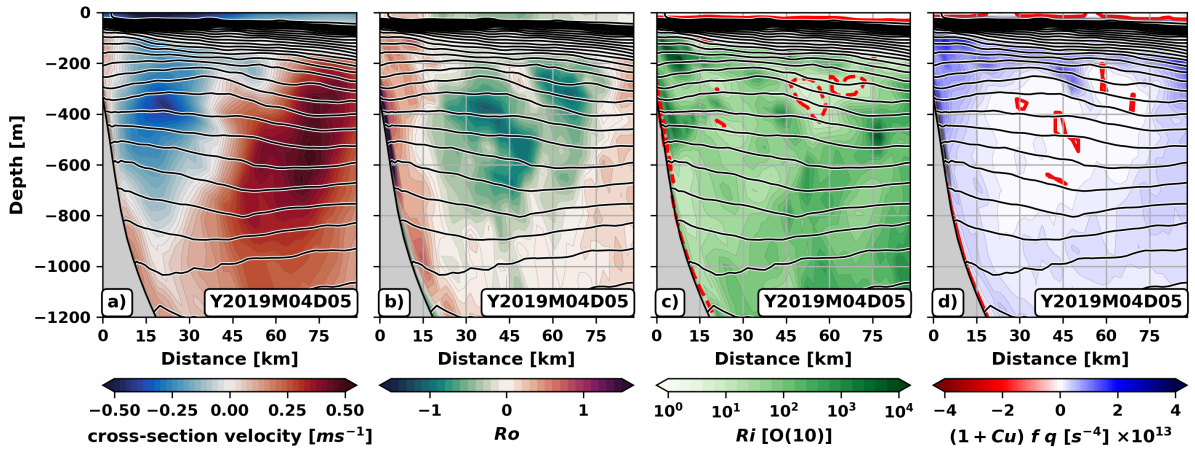

Figure 3.13: Vertical sections of the cross-section velocity (1^{st} column), the Rossby number (2^{nd} column), the Richardson number (3^{rd} column), and $(1+Cu)fq$ (4^{th} column) at the black transect crossing the mesoscale anticyclone displayed on Figures 3.12c and 3.12f. Black solid contours show isopycnals. Red solid and dashed contours on panel c show the lower and upper limits, respectively, of $\mathcal{O}(1)$ Richardson number. Red solid isolines on panel d show the $(1 + Cu)fq = 0$ contour.

In summary, our results indicate that anticyclonic SCVs can be generated by the interaction of BC meanders with the continental margin. These SCVs are triggered by inertial/symmetric instability and remain with negative/low $(1 + Cu)fq$ waters for several days. Some can evolve into mesoscale eddies, while others can be destroyed when hitting the western boundary. The lifetime of these SCVs is smaller than those advected by the large-scale flow in the interior ocean (e.g., Dewar & Meng, 1995; Lazaneo et al., 2022). However, they play an important role in cascading energy to both larger and smaller scales. In fact, Lazaneo et al. (2022) observed that anticyclonic SCVs can lead to kinetic energy dissipation in the interior ocean. Therefore, the SCVs described here may constitute an important sink of energy for the Brazil Current.

4 Summary and Conclusions

In this study, we use a submesoscale-permitting CROCO simulation to investigate submesoscale shear instabilities associated with Brazil Current (BC) cyclones generated between 22°S and 23°S. Our results indicate that the arrival of anticyclones upstream of separation regions ignites barotropic shear instability from 100 m to 300 m and, consequently, triggers the formation of BC cyclones downstream. The shear between the incoming anticyclone and the slope keeps generating barotropic shear instability and ejects amplified cyclonic filaments and submesoscale vortices offshore. Such submesoscale features keep feeding the mesoscale meanders and contribute to their growth in a submesoscale-to-mesoscale inverse cascade (e.g., Molemaker et al., 2015). The submesoscale cyclones span the upper 600 m with radii of ∼20 km, present $\mathcal{O}(1)$ Rossby numbers, and yield 50-100 m d^{-1} vertical velocities. Thus, their impact on the vertical exchange of tracers and the biogeochemical dynamics within the BC meanders is a topic that should be addressed in future studies.

In lower-resolution simulations, the generation of BC meanders occurs similarly, but through balanced dynamics (e.g., Molemaker et al., 2015). Nonetheless, when the submesoscale dynamics is not taken into account, energy conversions are approximately two orders of magnitude smaller (Appendix B). In fact, downscaling from eddy-resolving to submesoscale-permitting simulations improves not only the simulated energetic levels, but also the predictability of observed CST eddies in operational models (Santana et al., 2020). Submesoscale processes are essential for the formation dynamics of the regional BC meanders.

After their generation, BC meanders trigger inertial and symmetrical instabilities adjacent to the slope. Between 100 m and 900 m, the interaction of the inshore limb of the cyclones with the slope increases the shear, amplifies anticyclonic vorticity, and reduces the Richardson number to $\mathcal{O}(1)$ values. This leads the product between potential vorticity and absolute angular momentum to become negative ($(1 + Cu)fq < 0$), and the flow becomes inertially and/or symmetrically unstable. Subsequently, anticyclonic filaments are ejected offshore and roll up into anticyclonic SCVs. These anticyclonic SCVs present a smaller lifetime than those generated in the interior ocean (e.g., Lazaneo et al., 2022). However, they play important roles in cascading energy to both larger and smaller scales. Some can evolve into subsurface mesoscale eddies, while others remain

marginally stable until being destroyed by the topograghy. SCVs can generate an important pathway to energy dissipation (Lazaneo et al., 2022). Therefore, even though they present small life cycles, the SCVs described here can be relevant to the sink of energy within ocean western boundaries.

The regional BC mesoscale cyclones impact coastal upwelling, cross-shelf water transport, and biogeochemical dynamics (Calado et al., 2010; Palóczy et al., 2014; Mill et al., 2015; Pereira et al., 2019). In this work, we have shown the importance of submesoscale shear instabilities to the formation process of these mesoscale meanders and the generation of associated submesoscale vortices. We are currently working to address: i) the origin of the anticyclones that trigger barotropic shear instability upstream of CST and CF, and; ii) the impact of submesoscale motions on the biogeochemical dynamics within the BC cyclones.

5 Appendix A - Model Evaluation

The simulation is evaluated by comparing the mean thermohaline and velocity structure with available data and reports from previous works. We use the post-spin-up period of 2016 to 2019 (Figure 5.1) to construct the model temporal averages. Figure 5.2a shows the annual mean TS diagrams from the simulation and the WOA18 climatology. We compute both TS averages within the area of interest of this study (red dashed box on Figure 2.1a). Results show that the simulation represents well the regional thermohaline mean structure observed in the World Ocean Atlas 2018 (WOA18) climatology. Figure 5.2b shows the mean cross-section velocity vertical section at the black transect on Figure 5.2a. Corroborating Napolitano et al. (2019) (Figure 1.3), we find that: i) the BC occupies the upper 200 m transporting 2 Sv and reaches - 0.5 ms^{-1} at its surface core; and ii) the IWBC transports 13.1 Sv and reaches 0.2 ms^{-1} at its 800 m core. Finally, we show that the simulation successfully represents CST and CF cyclones events (Figure 5.3) as the observed by Mill et al. (2015), Pereira et al. (2019) and Silveira et al. (2020).

Lastly, we need to confirm that the simulation is submesoscale-permitting. To achieve that, we examine snapshots and the probability density function (PDF) of the following properties (e.g., Napolitano et al., 2021b):

$$Rossby\ number = Ro = \frac{\zeta}{f}, \tag{5.1}$$

$$strain\ rate = \frac{\alpha}{|f|} = \frac{\left[\left(\frac{\partial u}{\partial x} - \frac{\partial v}{\partial y}\right)^2 + \left(\frac{\partial v}{\partial x} + \frac{\partial u}{\partial y}\right)^2\right]^{\frac{1}{2}}}{|f|}, \tag{5.2}$$

$$divergence\ rate = \frac{\delta}{|f|} = \frac{\frac{\partial u}{\partial x} + \frac{\partial v}{\partial y}}{|f|}, \tag{5.3}$$

$$horizontalbuoyancygradientrate = \frac{M^2}{f^2} = \frac{|\nabla_h b|}{f^2}, \tag{5.4}$$

where ζ is the relative vorticity, f is the planetary vorticity, b is buyoancy, and u, v and w are

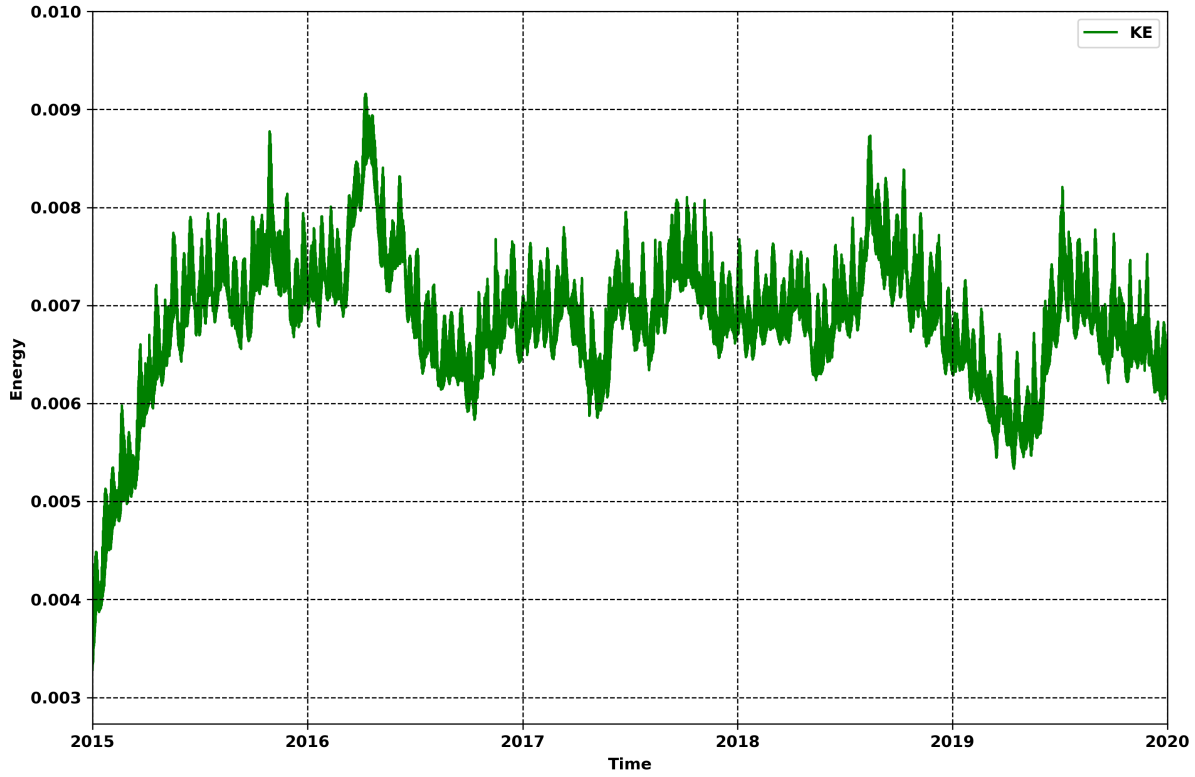

Figure 5.1: Kinetic Energy temporal evolution during the simulation. The spin-up of the run occurs in 2015.

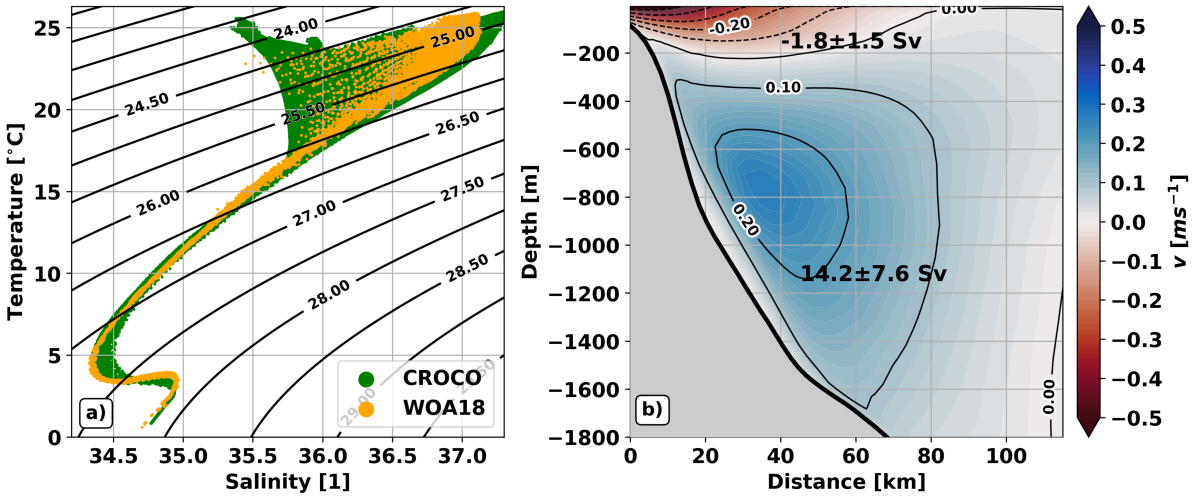

Figure 5.2: a) Temporal average of TS diagrams for the WOA18 climatology and the CROCO simulation computed within the area of interest (red dashed box on Figure 2.1a). b) Temporal average of cross-section velocity at the black transect from Figure 2.1a.

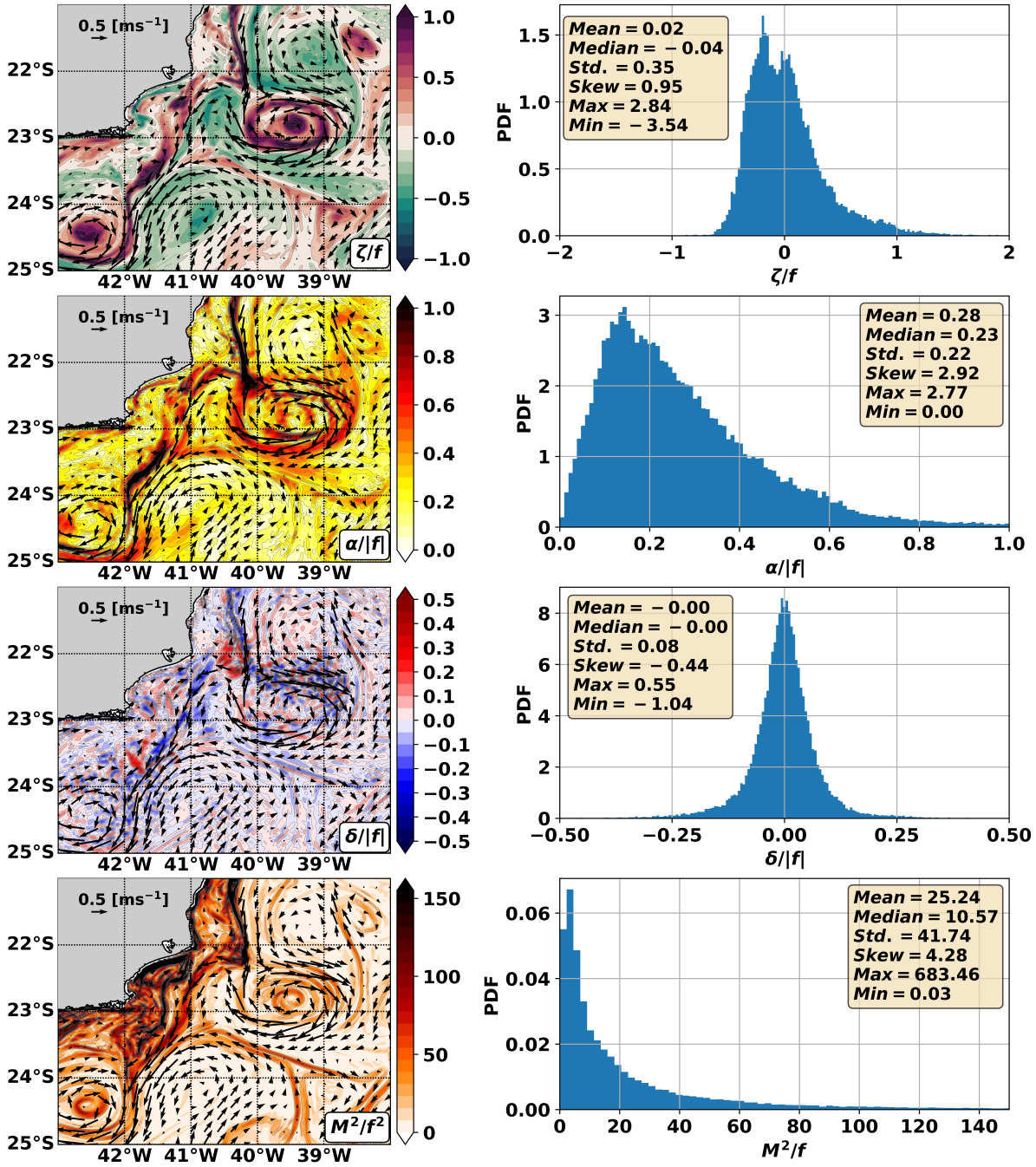

Figure 5.3: Horizontal distributions in March 20, 2017 at 10 m (left column) and their respective PDFs (right column) of the: 1^{st} row) Ro; 2^{nd} row) strain rate; 3^{rd} row) divergence rate; and, 4^{th} row) gradb. Horizontal velocities are also displayed on the horizontal maps (left column).

the zonal, meridional and vertical velocities, respectively.

The snapshots at 10 m and the correspondent PDFs of these properties reveal typical characteristics of submesoscale motions in accordance with Shcherbina et al. (2013) and Napolitano et al. (2021b) (Figure 5.3). The Rossby number, the strain rate, and the divergence rate reach $\mathcal{O}(1)$ values on the edges and in the center of the CST and CF cyclones (Figure 5.3). The Ro PDF shows large asymmetry with a typical tail towards cyclonic motions (skewness of 0.95), the divergence rate PDF shows a typical tail towards convergence (skewness of -0.44), and the strain rate PDF follows a χ^2 distribution (mean of 0.28 and skew of 2.92) with a tail of sporadic $\mathcal{O}(1)$ values. We observe that our simulation generates $M^2 f^{-2}$ extremes from 150 to 683 values, which correspond to M^2 values between $5{\times}10^{-7} s^{-2}$ and $2{\times}10^{-6} s^{-2}$. These strong buoyancy gradients are in accordance with studies that investigate submesoscale motions (e.g., Thomas et al., 2016; McWilliams et al., 2019; Napolitano et al., 2021b). Finally, these results show that our simulation is indeed submesoscale-permitting.

6 Appendix B - OfES Study Case

To verify how the generation of BC meanders occurs in models that do not permit the submesoscale dynamis, we perform a study case using OfES outputs (Masumoto et al., 2004; Sasaki et al., 2008). OfES is a model based on Modular Ocean Model ver.3. (Pacanowski & Griffies, 2000), developed by the Geophysical Fluid Dynamics Laboratory/National Oceanic and Atmospheric Administration. OfES is the result of a code designed to solve an Ocean General Circulation Model (OGCM) optimized for massive and parallel calculations in the "Earth Simulator" (OfES: OGCM for the Earth Simulator) developed by the JAMSTEC (Japan Agency for Marine-Earth Science and Technology).

OfES uses z-level vertical coordinates and solves three-dimensional primitive equations in spherical coordinates under the Boussinesq and hydrostatic approximations (Sasaki et al., 2008). The model domain spans from 75°S to 75°N and it uses 54 vertical levels with 0.1° horizontal resolution (Sasaki et al., 2008). Furthermore, it is run between 1950 and 2003 (Masumoto et al., 2004) with climatological forcing derived from NCEP/NCAR reanalysis products (Kalnay et al., 1996).

In our study case, we investigate a CST cyclone event that occurs in July-August 1992 (Figure 6.1). As seen in the CROCO simulation, we observe that the CST eddy is generated after an anticyclone reaches the continental slope upstream. We also observe the amplification and ejection of an amplified patch of cyclonic vorticity, but Ro does not exceed 0.1 in this case. This indicates that the dynamics of formation of the BC meanders is balanced in this eddy-resolving model.

We apply the energy conversions analysis to this event in order to check if barotropic and baroclinic instabilities still happen in this eddy-resolving simulation scenario. According to our results and corroborating Magalhães et al. (2017), we detect the occurrence of: i) barotropic instability upstream (positive HSP; Figures 6.2a-c), and; ii) baroclinic instability downstream (positive BP and BF; Figures 6.2f and 6.2i). The main difference between the CROCO and the OfES simulations is that the dynamics of this process is unbalanced in the submesoscale-permitting model and balanced in the eddy-resolving model (e.g., Molemaker et al., 2015). Consequently, we observe energy conversions approximately two orders of magnitude smaller in

the OfES simulation.

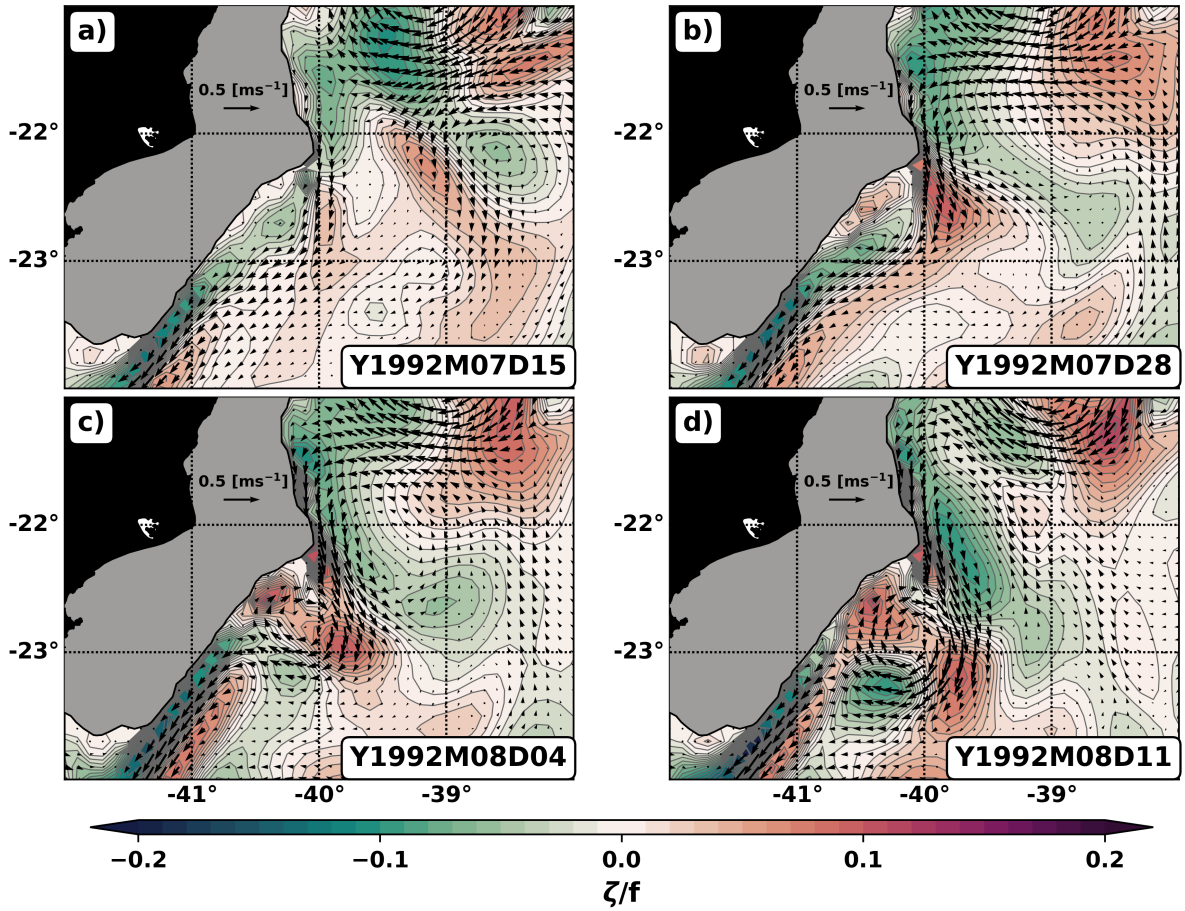

Figure 6.1: Horizontal distributions of ζ/f at 160 m during a CST cyclone event simulated by OfES.

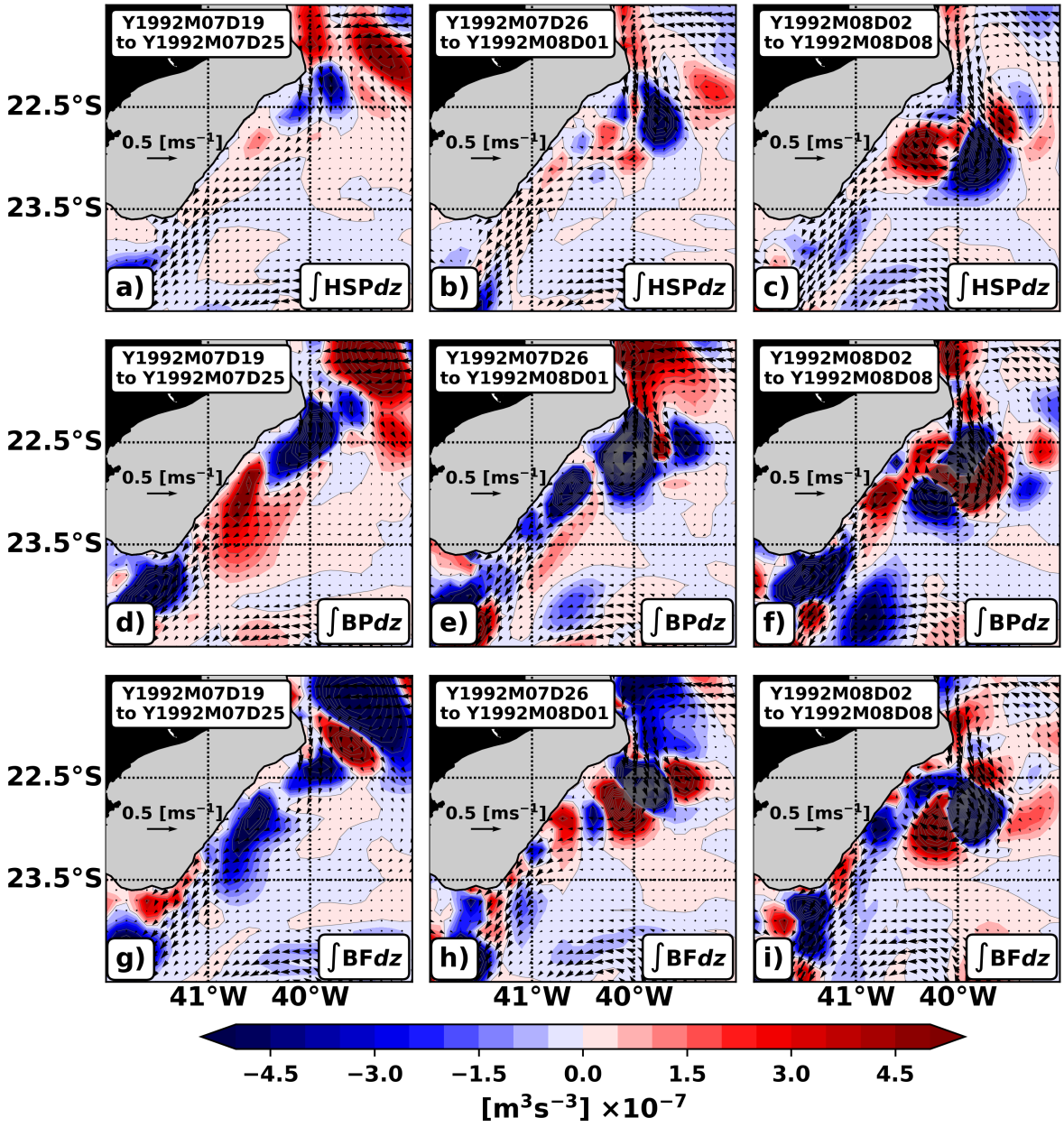

Figure 6.2: Energy analysis for the OfES CST cyclone 1992 event shown on Figures 6.1. Horizontal distributions of the vertically-integrated (100 m to 300 m) HSP (1^{st} row), BP (2^{nd} row), and BF (3^{rd} row). The 1^{st} column shows the period between July 19 to 25, the 2^{nd} column the period between July 26 to August 1, and the 3^{rd} column the period between August 2 to 8.

7 Publications

During my time as an IO-USP master's student, I was able to publish two research papers derived from my Bachelor's thesis. These studies are listed below.

7.1 Revisiting the Atlantic South Equatorial Current

Luko, C. D., Silveira, I. C. A., Simoes-Sousa, I. T., Araujo, J. M., & Tandon, A. (2021). Revisiting the Atlantic South Equatorial current. Journal of Geophysical Research: Oceans, 126(7). https://doi.org/10.1029/2021jc017387

Abstract

The southern branch of the South Equatorial Current (SSEC) is the northern limit of the South Atlantic Subtropical Gyre. When this current reaches Brazil around 14°S it bifurcates into a southward flow as the Brazil Current (BC) and the surface portion of the northward flowing North Brazil Undercurrent (NBUC). The SSEC system is a key component of the western boundary supply, influencing the NBUC/BC variability and, therefore, global climate through the Meridional Overturning Circulation. In this study, using altimetry satellite data and reanalyses outputs (1993-2018), we revisit the SSEC mean state and show this current arriving at the South Atlantic western boundary as a multi-banded flow with surface signatures resulting from different subsurface cores. These bands have velocities between 0.02 and 0.07 m s^{-1} and, as shown by ADCP data from the PIRATA project, their signature in synoptic scenarios is obscured by eddies and waves with velocities between 0.1 and 0.3 m s^{-1}. In addition, the SSEC annual cycle analysis shows that the seasonality of the bands is out of phase with each other, presenting westward transport anomalies between 0.4 and 2.6Sv. Finally, our results show that the seasonality of this multi-banded flow both defines where the BC is born, and modulates the seasonality of semi-permanent mesoscale eddies off Brazil.

7.2 Effects of the seasonality of mesoscale eddies on the planktonic dynamics off eastern Brazil

Luko, C. D., Pereira, F., Silveira, I. C. A., Tandon, A & Flierl, G. F. (2022). Effects of the seasonality of mesoscale eddies on the planktonic dynamics off eastern Brazil. Dynamics of Atmospheres and Oceans, 98, 101 299. https://doi.org/10.1016/j.dynatmoce.2022.101299

Abstract

The South Equatorial Current's southern branch (SSEC) reaches the Brazilian continental margin through several bands between 30° S and 10° S. As the SSEC 14° S band reaches the Brazilian continental margin, it bifurcates into the poleward-flowing Brazil Current (BC), and the surface portion of the equatorward-flowing North Brazil Undercurrent (NBUC). Some semi-permanent eddies are formed in association with the bifurcation, and their variability is controlled by the seasonality of the SSEC bands. This work aims to investigate the role of the seasonality of these mesoscale eddies on the regional phytoplanktonic dynamics. We analyze chlorophyll-a satellite observations and perform two experiments using a Nutrients-Phytoplankton-Zooplankton (NPZ) model coupled to a $1\frac{1}{2}$-layer quasi-geostrophic model. The results show that the phytoplankton annual cycle off eastern Brazil is mainly controlled by the seasonally varying advection of material offshore caused by the mesoscale eddies. Such a mechanism may represent an important source of material to the tropical oligotrophic ocean.

Bibliography

Aluie, H., Hecht, M., Vallis, G. K., 2018. Mapping the energy cascade in the North Atlantic Ocean: The coarse-graining approach. Journal of Physical Oceanography 48 (2), 225–244.

Buckingham, C., 2021. Submesoscale potential vorticity. Earth and Space Science Open Archive, 20.
URL https://doi.org/10.1002/essoar.10508902.1

Buckingham, C. E., Gula, J., Carton, X., 2021a. The role of curvature in modifying frontal instabilities. part I: review of theory and presentation of a nondimensional instability criterion. Journal of Physical Oceanography 51 (2), 299–315.

Buckingham, C. E., Gula, J., Carton, X., 2021b. The role of curvature in modifying frontal instabilities. Part II: Application of the criterion to curved density fronts at low Richardson numbers. Journal of Physical Oceanography 51 (2), 317–341.

Calado, L., Silveira, I. C. A., Gangopadhyay, A., Castro, B. M., 2010. Eddy-induced upwelling off Cape São Tomé (22 S, Brazil). Continental Shelf Research 30 (10-11), 1181–1188.

Chen, R., Flierl, G. R., Wunsch, C., 2014. A description of local and nonlocal eddy–mean flow interaction in a global eddy-permitting state estimate. Journal of Physical Oceanography 44 (9), 2336–2352.

Dewar, W. K., Meng, H., 1995. The propagation of submesoscale coherent vortices. Journal of physical oceanography 25 (8), 1745–1770.

Fadeev, E., Wietz, M., von Appen, W.-J., Iversen, M. H., Nöthig, E.-M., Engel, A., Grosse, J., Graeve, M., Boetius, A., 2021. Submesoscale physicochemical dynamics directly shape bacterioplankton community structure in space and time. Limnology and Oceanography.

Fox-Kemper, B., Ferrari, R., Hallberg, R., 2008. Parameterization of mixed layer eddies. Part I: Theory and diagnosis. Journal of Physical Oceanography 38 (6), 1145–1165.

Gula, J., Molemaker, M., McWilliams, J., 2015. Topographic vorticity generation, submesoscale instability and vortex street formation in the gulf stream. Geophysical Research Letters 42 (10), 4054–4062.

Gula, J., Molemaker, M. J., McWilliams, J. C., 2016a. Submesoscale dynamics of a Gulf Stream frontal eddy in the South Atlantic Bight. Journal of Physical Oceanography 46 (1), 305–325.

Gula, J., Molemaker, M. J., McWilliams, J. C., 2016b. Topographic generation of submesoscale centrifugal instability and energy dissipation. Nature communications 7 (1), 1–7.

Gula, J., Taylor, J., Shcherbina, A., Mahadevan, A., 2022. Submesoscale processes and mixing. In: Ocean Mixing. Elsevier, pp. 181–214.

Haney, R. L., 1991. On the pressure gradient force over steep topography in sigma coordinate ocean models. Journal of physical Oceanography 21 (4), 610–619.

Houry, S., Dombrowsky, E., De Mey, P., Minster, J.-F., 1987. Brunt-Väisälä frequency and Rossby radii in the South Atlantic. Journal of Physical Oceanography 17 (10), 1619–1626.

Kalnay, E., Kanamitsu, M., Kistler, R., Collins, W., Deaven, D., Gandin, L., Iredell, M., Saha, S., White, G., Woollen, J., et al., 1996. The NCEP/NCAR 40-year reanalysis project. Bulletin of the American meteorological Society 77 (3), 437–472.

Lazaneo, C. Z., Calil, P. H. R., Tandon, A., Silveira, I. C. A., 2022. Submesoscale coherent vortices in the South Atlantic Ocean: A pathway for energy dissipation. Journal of Geophysical Research: Oceans, e2020JC017099.

Lazaneo, C. Z., Napolitano, D. C., da Silveira, I. C. A., Tandon, A., MacDonald, D. G., Ávila, R. A., Calil, P. H. R., 2020. On the role of turbulent mixing produced by vertical shear between the Brazil Current and the Intermediate Western Boundary Current. Journal of Geophysical Research: Oceans 125 (1), e2019JC015338.

Lévy, M., Franks, P. J. S., Smith, K. S., 2018. The role of submesoscale currents in structuring marine ecosystems. Nature communications 9 (1), 1–16.

Luko, C. D., Silveira, I. C. A., Simoes-Sousa, I. T., Araujo, J. M., Tandon, A., 2021. Revisiting the atlantic south equatorial current. Journal of Geophysical Research: Oceans 126 (7), e2021JC017387.

Magalhães, F. C., Azevedo, J. L. L., Oliveira, L. R., 2017. Energetics of eddy-mean flow interactions in the B razil current between 20° S and 36° S. Journal of Geophysical Research: Oceans 122 (8), 6129–6146.

Mahadevan, A., 2016. The impact of submesoscale physics on primary productivity of plankton. Annual review of marine science 8, 161–184.

Masumoto, Y., Sasaki, H., Kagimoto, T., Komori, N., Ishida, A., Sasai, Y., Miyama, T., Motoi, T., Mitsudera, H., Takahashi, K., et al., 2004. A fifty-year eddy-resolving simulation of the world ocean: Preliminary outcomes of OFES (OGCM for the Earth Simulator). J. Earth Simulator 1, 35–56.

McWilliams, J. C., 2016. Submesoscale currents in the ocean. Proceedings of the Royal Society A: Mathematical, Physical and Engineering Sciences 472 (2189), 20160117.

McWilliams, J. C., Gula, J., Molemaker, M. J., 2019. The gulf stream north wall: Ageostrophic circulation and frontogenesis. Journal of Physical Oceanography 49 (4), 893–916.

Mill, G. N., Costa, V. S., Lima, N. D., Gabioux, M., Guerra, L. A. A., Paiva, A. M., 2015. Northward migration of Cape São Tomé rings, Brazil. Continental Shelf Research 106, 27–37.

Molemaker, M. J., McWilliams, J. C., Dewar, W. K., 2015. Submesoscale instability and generation of mesoscale anticyclones near a separation of the California Undercurrent. Journal of Physical Oceanography 45 (3), 613–629.

Morvan, M., L'Hégaret, P., Carton, X., Gula, J., Vic, C., de Marez, C., Sokolovskiy, M., Koshel, K., 2019. The life cycle of submesoscale eddies generated by topographic interactions. Ocean Science 15 (6), 1531–1543.

Müller, P., McWilliams, J. C., Molemaker, M. J., 2005. Routes to dissipation in the ocean: The 2D/3D turbulence conundrum. Marine turbulence: theories, observations and models 397, 405.

Napolitano, D. C., Rocha, C. B., Silveira, I. C. A., Simoes-Sousa, I. T., Flierl, G. R., 2021a. Can the Intermediate Western Boundary Current recirculation trigger the Vitória Eddy formation? Ocean Dynamics, 1–12.

Napolitano, D. C., Silveira, I. C. A., Rocha, C. B., Flierl, G. R., Calil, P. H. R., Martins, R. P., 2019. On the steadiness and instability of the intermediate western boundary current between 24 and 18 S. Journal of Physical Oceanography 49 (12), 3127–3143.

Napolitano, D. C., Silveira, I. C. A., Tandon, A., Calil, P. H. R., 2021b. Submesoscale phenomena due to the Brazil Current crossing of the Vitória-Trindade Ridge. Journal of Geophysical Research: Oceans 126 (1), e2020JC016731.

Pacanowski, R. C., Griffies, S. M., 2000. The MOM3 manual. GFDL Ocean Group Technical Report 4. Geophysical Fluid Dynamics Laboratory, Princeton, NJ.

Palóczy, A., Silveira, I. C. A., Castro, B. M., Calado, L., 2014. Coastal upwelling off Cape São Tomé (22 S, Brazil): The supporting role of deep ocean processes. Continental Shelf Research 89, 38–50.

Pedlosky, J., et al., 1987. Geophysical fluid dynamics. Vol. 710. Springer.

Pereira, F., Silveira, I. C. A., Flierl, G. R., Tandon, A., 2019. NPZ response to eddy-induced upwelling in a Brazil Current ring: A theoretical approach. Dynamics of Atmospheres and Oceans 87.

Rocha, C. B., Silveira, I. C. A., Castro, B. M., Lima, J. A. M., 2014. Vertical structure, energetics, and dynamics of the Brazil Current System at 22 S–28 S. Journal of Geophysical Research: Oceans 119 (1), 52–69.

Rodrigues, R. R., Rothstein, L. M., Wimbush, M., 2007. Seasonal variability of the South Equatorial Current bifurcation in the Atlantic Ocean: A numerical study. Journal of Physical Oceanography 37 (1), 16–30.

Santana, R., Costa, F. B., Mignac, D., Santana, A. N., Vidal, V. F. d. S., Zhu, J., Tanajura, C. A., 2020. Model sensitivity experiments on data assimilation, downscaling and tides for the representation of the Cape São Tomé Eddies. Ocean Dynamics 70 (1), 77–94.

Sasaki, H., Nonaka, M., Masumoto, Y., Sasai, Y., Uehara, H., Sakuma, H., 2008. An eddy-resolving hindcast simulation of the quasiglobal ocean from 1950 to 2003 on the Earth Simulator. In: High resolution numerical modelling of the atmosphere and ocean. Springer, pp. 157–185.

Schmid, C., Majumder, S., 2018. Transport variability of the Brazil Current from observations and a data assimilation model. Ocean Science 14 (3), 417–436.

Schubert, R., Gula, J., Biastoch, A., 2021. Submesoscale flows impact Agulhas leakage in ocean simulations. Communications Earth & Environment 2 (1), 1–8.

Schubert, R., Gula, J., Greatbatch, R. J., Baschek, B., Biastoch, A., 2020. The submesoscale kinetic energy cascade: Mesoscale absorption of submesoscale mixed layer eddies and frontal downscale fluxes. Journal of Physical Oceanography 50 (9), 2573–2589.

Schubert, R., Rath, W., 2021. reneschubert/keflux: Computing the oceanic kinetic energy flux across spatial scales using coarse-graining (Version v.1.0.1).
URL `https://doi.org/10.5281/zenodo.4486265`

Shchepetkin, A. F., McWilliams, J. C., 2005. The regional oceanic modeling system (ROMS): a split-explicit, free-surface, topography-following-coordinate oceanic model. Ocean modelling 9 (4), 347–404.

Shcherbina, A. Y., D'Asaro, E. A., Lee, C. M., Klymak, J. M., Molemaker, M. J., McWilliams, J. C., 2013. Statistics of vertical vorticity, divergence, and strain in a developed submesoscale turbulence field. Geophysical Research Letters 40 (17), 4706–4711.

Silveira, I. C. A., Calado, L., Cirano, M., Castro, B. M. d., Lima, J. A., Mascarenhas, A. D. S., 2004. On the baroclinic structure of the Brazil Current-Intermediate Western Boundary Current system at 22-23 S. Geophysical Research Letters 31, 1–5.

Silveira, I. C. A., Lima, J. A. M., Schmidt, A. C. K., Ceccopieri, W., Sartori, A., Franscisco, C. P. F., Fontes, R. F. C., 2008. Is the meander growth in the Brazil Current system off Southeast Brazil due to baroclinic instability? Dynamics of Atmospheres and Oceans 45 (3-4), 187–207.

Silveira, I. C. A., Napolitano, D. C., Farias, I. U., 2020. Water masses and oceanic circulation of the Brazilian continental margin and adjacent abyssal plain. In: Brazilian Deep-Sea Biodiversity. Springer, pp. 7–36.

Soufflet, Y., Marchesiello, P., Lemarié, F., Jouanno, J., Capet, X., Debreu, L., Benshila, R., 2016. On effective resolution in ocean models. Ocean Modelling 98, 36–50.

Soutelino, R. G., Silveira, I. C. A., Gangopadhyay, A., Miranda, J. A., 2011. Is the Brazil Current eddy-dominated to the north of 20 S? Geophysical Research Letters 38 (3).

Stramma, L., England, M., 1999. On the water masses and mean circulation of the South Atlantic Ocean. Journal of Geophysical Research: Oceans 104 (C9), 20863–20883.

Theisel, H., Rauschenbach, U., 1999. Curvis-visualizing the curvature of vector fields on the internet. Rostocker Informatik-Berichte 23, 105–114.

Thomas, L. N., Tandon, A., Mahadevan, A., 2008. Submesoscale processes and dynamics. Ocean modeling in an Eddying Regime 177, 17–38.

Thomas, L. N., Taylor, J. R., D'Asaro, E. A., Lee, C. M., Klymak, J. M., Shcherbina, A., 2016. Symmetric instability, inertial oscillations, and turbulence at the Gulf Stream front. Journal of Physical Oceanography 46 (1), 197–217.

Thomas, L. N., Taylor, J. R., Ferrari, R., Joyce, T. M., 2013. Symmetric instability in the Gulf Stream. Deep Sea Research Part II: Topical Studies in Oceanography 91, 96–110.

Wenegrat, J. O., Callies, J., Thomas, L. N., 2018. Submesoscale baroclinic instability in the bottom boundary layer. Journal of Physical Oceanography 48 (11), 2571–2592.